



A graph neural network approach to basin-scale river network learning: The role of physics-based connectivity and data fusion

Alexander Y. Sun¹, Peishi Jiang², Zong-Liang Yang³, Yangxinyu Xie⁴, and Xingyuan Chen²

¹Bureau of Economic Geology, The University of Texas at Austin, Austin, TX, USA

²Pacific Northwest National Laboratory, Richland, WA, USA

³Department of Geological Sciences, The University of Texas at Austin, Austin, TX, USA

⁴Department of Computer Science, The University of Texas at Austin, Austin, TX, USA

Correspondence: Alexander Y. Sun (alex.sun@beg.utexas.edu)

Abstract. Rivers and river habitats around the world are under sustained pressure from anthropogenic activities and the changing global environment. Our ability to quantify and manage the river states in a timely manner is critical for protecting the public safety and natural resources. Vector-based river network models have enabled modeling of large river basins at increasingly fine resolutions, but are computationally demanding. This work presents a multistage, physics-guided, graph neural network (GNNs) approach for basin-scale river network learning and stream forecasting. GNN models are pretrained using a high-resolution vector-based river network model, and then fine-tuned with in situ streamflow observations, after which a post-processing data fusion step is proposed to propagate residuals over the entire network to correct predictions. The GNN-based framework is demonstrated over a snow-dominated watershed in the western U.S. consisting of 552 reaches. A series of experiments are performed to test different training and imputation strategies. Results show the trained GNN model can effectively serve as a surrogate model of the process-based model with high accuracy, with median Kling–Gupta efficiency (KGE) greater than 0.97. Application of the graph-based data fusion further reduces mismatch between the GNN model and observations, with as much as 50 percent KGE improvement over some cross-validation gages. Additionally we exploit and demonstrate a graph coarsening procedure that achieves comparable predicting skills at only a fraction of training cost, thus providing important insights on the degree of physical realism needed for developing large-scale GNN-based river network models.

1 Introduction

Rivers play a critical role in the hydrosphere, enabling and regulating hydrological, geomorphic and ecological processes along and adjacent to the riverine environment (De Groot et al., 2002; Dai and Trenberth, 2002). Rivers



around the world are also under sustained pressure from human activities, losing free-flowing connectivity over time due to the construction of dams, levees, and other hydroinfrastructures for providing societal goods and services (e.g., hydropower generation) (Best, 2019). About half of the global river reaches now show signs of diminished connectivity (Grill et al., 2019). The changing climate and population growth further exacerbate the existing stress
25 on river systems by modulating the spatial and temporal patterns of floods and droughts, including their frequency, magnitude and timing (Winsemius et al., 2016; Blöschl et al., 2017; Dottori et al., 2018), and by reducing the rivers' natural ability to absorb disturbances and buffer the ecosystem (Palmer et al., 2008). Thus, our ability to quantify and manage the river states and fluxes in a timely manner has become more important than ever for protecting the public safety and adapting to the changing environment. Stream gauges can provide direct measures of river
30 discharges, but the utility of which is hindered by the poor coverage of gauge networks in many parts of the world. Instead, hydrological models are broadly used to predict river discharges at ungauged locations (Hrachowitz et al., 2013; Beck et al., 2015).

The fidelity of a hydrological model hinges on a number of factors, including the accuracy of forcing data, soundness of process parameterization, and the realism of river network geometry used in the model (Bierkens et al., 2015).
35 In many distributed and semi-distributed models, river networks are delineated on the same grid as the underlying hydrological models or land surface models (Döll et al., 2003; Van Beek et al., 2011; Pokhrel et al., 2012; Alfieri et al., 2013). Prescribing river networks over coarse resolution grids may introduce misrepresentation in river routing models, leading to inaccurate river discharge estimates and misalignment with local application needs (Zhao et al., 2017; Mizukami et al., 2021). While representation of river networks can always be improved by refining the grid
40 resolution, in reality such effort is often constrained by computational resources, especially for large scale simulations (Yamazaki et al., 2013; Bierkens et al., 2015).

In the past decade, vector hydrography has (re)emerged as an alternative to the conventional grid-based approaches for large river basin simulations (David et al., 2011; Lehner and Grill, 2013; Yamazaki et al., 2013; Lin et al., 2018). In a vector network representation, the land surface of a river basin is discretized into unit catchments (polygons)
45 and the river reaches connecting them by using a high-resolution digital elevation model (Saunders, 2000). Unlike the grid-based representation, in a vector-based river model the unit catchments serve as calculation units, and the time evolution of state variables is solved by calculating the flux exchange between each unit catchment and the next downstream unit catchment along a prescribed river network (Yamazaki et al., 2013). Direct benefits of such a discretization scheme are (a) river geometries are realistically represented; (b) river reach distances are relatively
50 evenly distributed, allowing for greater computing time steps and thus gaining more computational efficiency; (c) the unit catchment resolution can be easily improved by applying more detailed polygon outlines; and (d) hydrologic features such as lakes and irrigation lines can be modeled as additional vector features attached to the catchments and river reaches (Mizukami et al., 2021).

The vector-based river representation is behind the National Water Model (NWM), which operationally generates
55 short- and long-range river discharge forecasts for more than 2.7 million reaches in the U.S. (Lin et al., 2018;



Salas et al., 2018). Vector-based river network simulations were also used to create validation datasets for the upcoming Surface Water and Ocean Topography (SWOT) satellite mission, designed to provide global observations of changing water levels in large rivers, lakes, and floodplains (Biancamaria et al., 2016; Lin et al., 2019). Despite their improved efficiency, vector-based river routing models are still computationally demanding, requiring special domain decomposition techniques for parallel computation (David et al., 2011; Mizukami et al., 2021)

The renewed interests in vector hydrography have been driven by an increased demand for hyperresolution terrestrial hydrology models on the one hand (Bierkens et al., 2015), and the deluge of high-resolution Earth observation data on the other (Sun and Scanlon, 2019; Reichstein et al., 2019). Ultimately, the Earth science community envisions the development of Earth system digital twins, aiming to provide digital replica of the real world through high-fidelity simulations and observations (Bauer et al., 2021). Toward that vision, two active veins of research are currently underway. One is continuously improving the physical realism of process representation within the current Earth system models at all scales and across all subsystem interfaces, which is a daunting task even with today's extreme-scale, high-performance computing power (Schulthess et al., 2018). The other is augmenting process-based models with artificial intelligence/machine learning (AI/ML) techniques, which has attracted significant attentions in the past several years (Shen, 2018; Sun and Scanlon, 2019; Reichstein et al., 2019; Camps-Valls et al., 2021; Kashinath et al., 2021; Pathak et al., 2022). Existing AI/ML works related to hydroclimate modeling may be classified as (a) data-driven techniques (Kratzert et al., 2019b; Le et al., 2021; Sun et al., 2021; Feng et al., 2021); (b) hybrid process-based/ML models (Rasp et al., 2018; Yuval and O'Gorman, 2020; Nonnenmacher and Greenberg, 2021); and (c) physics-guided, post-processing (PGPP) techniques (Ham et al., 2019; Sun et al., 2019; Yang et al., 2019; Feng et al., 2020; Willard et al., 2020; Lu et al., 2021; Kashinath et al., 2021; Pathak et al., 2022). Although in the literature the latter two categories are sometimes combined, in the context of this discussion the former category is seen as providing ML-based parameterization schemes (e.g., subgrid processes) within a process-based model (Rasp et al., 2018; Reichstein et al., 2019), while the latter category mainly leverages outputs of process-based models and first-order physics principles in an ad hoc manner. ML-based PGPP methods can provide added values to existing process models, such as improved predictability, reduced bias, and/or computational efficiency, without requiring significant modifications to the existing scientific computing workflows and codes. This largely explains the popularity of PGPP paradigm in the Earth science community.

So far, only a few studies have exploited the use of ML in vector hydrography. This is partly because many of the deep learning techniques in use today are originated from the computer vision and natural language processing literature, dealing mostly with gridded or sequence data. On the other hand, many types of data in natural and social sciences, such as weather stations, river networks, and social networks, are characterized by graph-like data structures (i.e., nodes and node links) that do not conform to the Euclidean geometry. Various graph neural network (GNN) models have been developed (Bruna et al., 2013; Kipf and Welling, 2016; Bronstein et al., 2017; Zhou et al., 2018) to learn the graph structured data. Like their counterpart for learning image-like data (e.g., convolutional neural networks or CNNs), GNNs are designed to extract high-level features from input data through the the so-



called neural message passing and aggregation process, consisting of a series of algebraic operations to progressively encode nodes' features and their local structures (e.g., the number of neighbors) as latent representations (i.e., low-dimensional embeddings) (Kipf and Welling, 2016; Hamilton et al., 2017). Parameters of the embeddings are then learned from the training data through back propagation. GNNs, when combined with temporal learning algorithms (e.g., recurrent neural network or RNN), comprise powerful tools for disentangling highly complex, spatial and temporal relationships. We point out that the graph theory, which is at the foundation of GNNs, has been widely applied in geosciences to model geological processes, for example, formation of river deltas (Phillips et al., 2015; Tejedor et al., 2018). However, GNNs focus more on learning the latent-space representations for downstream tasks (e.g., classification and regression) than on abstracting graph-level statistics, as commonly done under most graph theoretic studies (Hamilton et al., 2017).

Jia et al. (2021) used a physics-guided, recurrent graph convolution network (GCN) model to predict streamflow and water temperature in a catchment of the Delaware River basin in the U.S. In their work, physics constraints are imposed in multiple ways: the actual river reach lengths and upstream/downstream connections are used to construct a weighted adjacency matrix; a process-based streamflow and water temperature model is used to generate synthetic training samples for ungauged reaches; and finally data collected from gauged locations are used in an extra loss term to enforce physical consistency with observations. The authors reported their recurrent GNN model generally gives better performance than a baseline RNN model, but may yield large errors at unobserved river reaches and reaches with extremely low flows. Sun et al. (2021) adapted and compared the performance of several recurrent GNN architectures for predicting streamflows of basins in the Catchment Attributes and Meteorology for Large-Sample Studies (CAMELS) dataset, which includes meteorological forcing, basin static attributes, and observed streamflow time series for 671 basins in the conterminous U.S. (Newman et al., 2015). The GNN algorithms they investigated include several basic GNNs, such as the GCN (Kipf and Welling, 2016) and ChebNet (Defferrard et al., 2016), as well as a more complex GNN model, the GraphWavenet (GWN for short) (Wu et al., 2019). They used hydrosimilarity as a distance measure to connect the spatially scattered basins, treating each basin and its static attributes as node and node features. Their results show the GWN gives the best overall performance, while models based on the basic GNN layers perform worse than a baseline model trained using the long short-term memory (LSTM) network (Hochreiter and Schmidhuber, 1997). Chen et al. (2021) adopted a heterogeneous recurrent graph model to predict stream temperatures, in which river reaches and dams are represented as separate graphs. For each river reach the authors used gating variables to control the information flow from upstream river reaches and reservoirs, in addition to the antecedent states of the river reach itself. Similar to (Jia et al., 2021), observations are incorporated directly in an extra loss term during training, as well as for adjusting the hidden states. These recent studies have demonstrated the potential of GNNs for vector-based river modeling. Specifically, GNNs may allow fine-grained control of information exchanges at the node and edge levels for incorporating the physical realism, an aspect that is missing in many other ML algorithms commonly used to model spatiotemporal datasets (e.g., random forests and



125 RNNs). In the remainder of this discussion, we shall use node and reach interchangeably when streamflow in the reach is implied.

Despite their potential promise, remaining questions pertaining to GNN applications in the vector hydrography are (a) the degree of physical realism that is needed for a GNN model to learn river network representations; (b) the generalization and scalability of GNN models, and (c) data fusion. To understand these research needs, we highlight the main differences between river networks and many other types of networks. River networks are hierarchical, with downstream discharges reflecting the integrated hydrologic contributions from all upstream reaches and catchments (Weiler et al., 2003). Reaches adjacent to each other tend to share similar runoff generation processes because of similarities in catchment physiographic properties and meteorological forcing. These unique aspects of river networks imply that information passing in a river network should be multi-directional, rather than strictly following the network topography as prescribed through the physics-based connectivity. Identifying and modeling the multi-directional and heterogeneous information transfer mechanisms using GNNs is an active research topic (Zhou et al., 2018). Perhaps a more practical question is related to graph generalization and scalability. The river networks considered in Jia et al. (2021) and Chen et al. (2021) include 42 and 56 river reaches, respectively, which are relatively small. In comparison, a typical basin at the U.S. Geological Survey's (USGS) 8-digit hydrological unit code (HUC-8) level contains $\mathcal{O}(10^2 - 10^3)$ river reaches, and at the largest HUC-2 regional basin level, the river network may include $\mathcal{O}(10^4 - 10^5)$ reaches (Simley and Carswell Jr, 2009). State-of-the-art GNN models have demonstrated capabilities to handle large scale graphs containing $\mathcal{O}(10^8)$ nodes on classification problems (Hu et al., 2020; Wang et al., 2021). Learning large-scale, vector river networks, however, is still a challenging topic because of the dynamic nature of the problem and computing memory requirements. A fruitful research direction may be exploring the graph sparsification or coarsening in a way that preserves the spatiotemporal structure of the river system. Finally, data fusion on graph-based, river network models has not been systematically studied, but represents an important class of post-processing techniques for watershed modeling. In general, post-processing techniques, as their names suggest, attempt to refine model outputs using new observations obtained after model simulations. In streamflow forecasting, post-processors have been used to correct the biases and dispersion errors in raw forecasts, downscale the forecasts to the scale of applications, and generate forecast ensembles that preserve the spatiotemporal structure of river discharges (Todini, 2008; Weerts et al., 2011; Li et al., 2017). Unlike data assimilation, data fusion as defined and used in the context of this work is generally decoupled from the original model.

In light of the aforementioned challenges, this study was conducted with the following two objectives in mind, namely, (a) evaluate the role of physics-based connectivity in GNN river network surrogate modeling, and (b) adapt and investigate the efficacy of a graph-based data fusion technique. Main contributions of this work are we have developed a methodology consisting of pretraining, fine-tuning, and data fusion steps to significantly improve the performance of GNN models; we show that the degree of realism required for a GNN surrogate model to catch spatiotemporal basin flow dynamics largely depends on the parameter structure of the underlying physics-based model. The remainder of this paper is organized as follows. In Section 2, we describe data and data processing techniques



160 used in this study. Section 3 focuses on the theoretical background of GNN and data fusion algorithms. Section 4
describes the demonstration study area and experimental design, which are followed by results and discussion in
Section 5 and conclusions in the last section.

2 Data and Data Processing

2.1 National Water Model

165 NWM is a continental-scale, distributed, hydrological modeling framework implemented and operated by the U.S.
National Weather Service for providing short-range (18 hour), medium-range (10 days) and long-range (30 days)
streamflow forecasts in the U.S. (Cosgrove et al., 2016). It is based on the WRF-Hydro community model, which is
both a standalone model and a coupling architecture to facilitate the exchange between the Weather Research and
Forecasting (WRF) atmospheric model and components of a land surface model (e.g., surface runoff, channel flow,
170 lake/reservoir flow, subsurface flow, and land-atmosphere exchanges) (Gochis et al., 2018). WRF-Hydro supports
surface runoff routing over vector-based river networks. The network topology used in NWM is derived from the
U.S. National Hydrography Dataset Plus (NHDPlus), a georeferenced, hydrologic dataset incorporating 1:100,000-
scale national stream network and a 30-m national digital elevation dataset, in addition to a large number of
river and catchment attributes for enhancing network analyses (McKay et al., 2012; Moore and Dewald, 2016). We
175 primarily used the NWM v2.0 retrospective simulation data that was available when this study was initiated. NWM
v2.0 contains NWM retrospective simulation outputs in hourly time steps at 2,729,076 NHDPlus reaches for the
period 1993/01/01–2018/12/31. As part of the sensitivity analysis, we also tested our approaches on NWM v2.1
retrospective data, which covers a longer 42-year period (1979/02/01–2020/12/31). A subset of NWM parameters
are calibrated by model developers using historical streamflow data at limited basins, but no nudging is applied on
180 the retrospective runs (Cosgrove et al., 2016). NWM v2.0 streamflow data is downloaded from a data server hosted
by Hydroshare (Johnson and Blodgett, 2020), while NWM 2.1 streamflow data is downloaded from National Oceanic
and Atmospheric Administration’s (NOAA) Amazon Web Services data repository (NOAA, 2022). Python scripts
are used to automate the remote subsetting and downloading of all NWM streamflow data for any U.S. basin of
interest. All data is aggregated into daily steps.

185 2.2 Meteorological forcing and streamflow

NWM v2.0 is driven by forcing data resampled from the North American Land Data Assimilation System (NLDAS),
which is originally available on a 1/8 degree grid (~14km at the equator) (Xia et al., 2012), while NWM v2.1 is driven
by the 1-km Analysis of Record for Calibration (AORC) dataset that is not publicly available at the time of this
writing (Kitzmilller et al., 2018). In this study, we used Daymet, which provides gauge-based, gridded estimates of
190 daily weather and climatology variables over the continental North America, including daily minimum and maximum



temperature, precipitation, vapor pressure, shortwave radiation, snow water equivalent (Thornton et al., 2012). The spatial resolution of Daymet is $1 \text{ km} \times 1 \text{ km}$ and the temporal coverage is from 1950 through the end of the most recent full calendar year. Although built upon similar gauge data, Daymet data is likely different from the meteorological forcing data used in NWM because of the different interpolation and extrapolation schemes used to
195 create it. Combining Daymet with antecedent NWM outputs as predictors may thus indirectly achieve the effect of using multiple forcing data, which has been shown to improve the generalization skill of Earth science ML models (Sun et al., 2019; Kratzert et al., 2021). Daymet data is downloaded by programmatically calling the Daymet web services (ORNL, 2022) and getting data closest to the centroid of each reach in a river network. Streamflow gage data is downloaded from USGS' National Water Information System by using the USGS Python package for water
200 data retrieval (USGS, 2022a).

2.3 River network construction

River network for a basin under study may be extracted from the NHDPlus database by performing the following steps. First, the NHDPlus v2.1 geodatabase covering the basin is downloaded from the U.S. Environmental Protection Agency (EPA) data server (EPA, 2022). The basin mask is used to crop the NHDFlow shape layer included in the
205 NHDPlus geodatabase, which is then joined with the PlusFlow table, also from NHDPlus. After this step, we have all reach attributes, including identification number of each river reach (referred to as COMID in NHDPlus), the upstream/downstream reaches of each reach, the reach type (e.g., stream or artificial path) and reach length, that are necessary for building a river network and populating the node features. We used a Python script to recursively traverse all river reaches to gather reach attributes and build the network (i.e., in terms of graph adjacency matrix).
210 The reach COMIDs corresponding to USGS gauge locations are also obtained for mapping purposes. All watershed boundaries used in this study are extracted from the Watershed Boundary Dataset, which includes basin boundaries at various HUC levels (USGS, 2022b). For the graph imputation/interpolation demonstration, we used the pour points corresponding to the HUC-12 basins (Price, 2022).

3 Methodology

215 We start by introducing some notations. A graph is represented by $\mathcal{G}(\mathcal{V}, \mathcal{E})$, where $\mathcal{V} = \{v_i\}_{i=1}^N$ is a set of N nodes and $\mathcal{E} = \{e_{ij}\}$ is a set of edges connecting node pairs (v_i, v_j) for $v_i \in \mathcal{V}$ and $v_j \in \mathcal{V}$. The neighborhood of a node is a subset of nodes connected to it, $\mathcal{N}(v) = \{u \in \mathcal{V} \mid (u, v) \in \mathcal{E}\}$. Node connections are specified by the adjacency matrix $\mathbf{A} \in \mathbb{R}^{N \times N}$, of which an element a_{ij} is equal to 1 if nodes v_i and v_j are connected and 0 otherwise. A graph can be either undirected (edge is bidirectional) or directed (edge direction matters). The adjacency matrix may also
220 be weighted, in which case elements of \mathbf{A} would be decimal numbers describing the affinity or similarity between two nodes. The graph feature matrix is denoted as $\mathbf{X} \in \mathbb{R}^{N \times D}$, with its rows representing node feature vectors

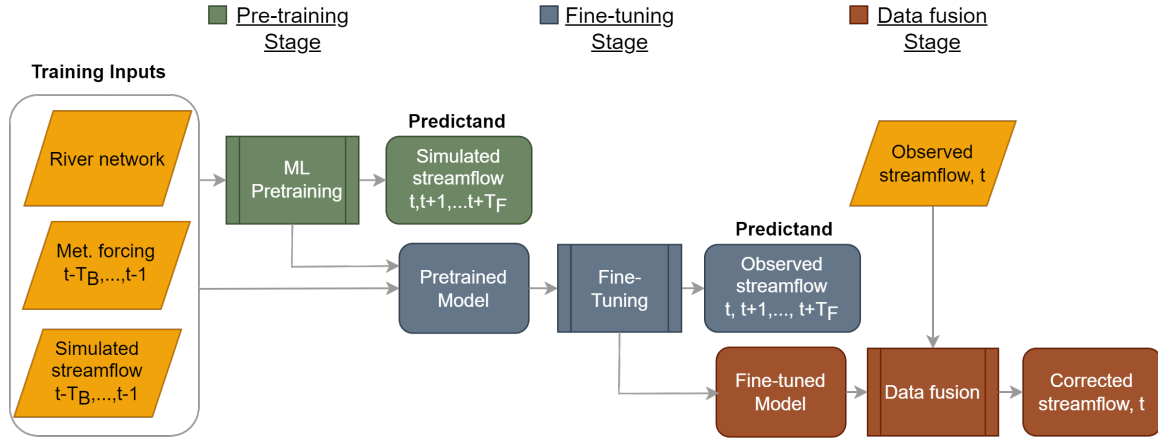


Figure 1. An ML-based workflow for basin-scale streamflow forecasting. The workflow consists of three stages, pretraining, fine-tuning, and data fusion. During pretraining, an ML model is trained to learn the input-output mapping as governed by the physics-based National Water Model. Inputs include river network attributes and connectivity, meteorological forcing, and antecedent simulated streamflow. The predictand is simulated streamflow, where T_B and T_F denote the lengths of lookback and forecast periods. In the fine-tuning step, the ML model is trained to minimize mismatch with historical streamflow observations. During data fusion, ML streamflow predictions are adjusted through graph-based residual propagation. Both pretraining and fine-tuning are performed offline, but data fusion can be done in real time.

$\mathbf{x}_i \in \mathbb{R}^D, i = 1, \dots, N$. In the dynamic setting considered in this work, the node features vary with time and the graph feature matrix is denoted by \mathbf{X}^t .

To develop a GNN-based, end-to-end framework for vector-based river network modeling, we propose a three-stage workflow as shown in Fig. 1. In Stage I, a GNN-based model is trained through supervised learning by using the meteorological forcing data and NWM outputs. This pretraining step is essentially a surrogate modeling process that learns the spatiotemporal rainfall-runoff patterns governed by NWM and meteorological forcing. The predictors include the six meteorological forcing variables from Daymet and the NWM simulated streamflow for a lookback period of T_B , as well as the adjacency matrix \mathbf{A} describing the river network connectivity. A neural network is trained to approximate the mapping $\mathcal{F}(\mathcal{X}^t, \mathbf{y}^t)$, where \mathcal{X}^t is a collation of predictors $\{\mathbf{X}^i\}_{i=t-T_B}^{t-1}$, $\mathbf{y}^t \in \mathbb{R}^N$ is the NWM outputs for the entire river network, and the forecast can be done for T_F steps in the future. In Stage II, a fine-tuning step is used to correct the pretrained GNN model by utilizing historical streamflow data available in the training period. The trained model can then be deployed for online prediction in Stage III, which uses data fusion to further correct GNN predictions based on residuals between predictions and observations. We describe these steps in details below.



3.1 Graph-based surrogate modeling for river networks

The GNN surrogate modeling framework used in this work is adapted from GraphWaveNet (GWN) (Wu et al., 2019), which consists of two types of interleaved layers, namely, GNN layers for spatial learning and temporal convolution network (TCN) layers for temporal learning. A schematic plot of the adapted GWN design is provided in Fig. 2.

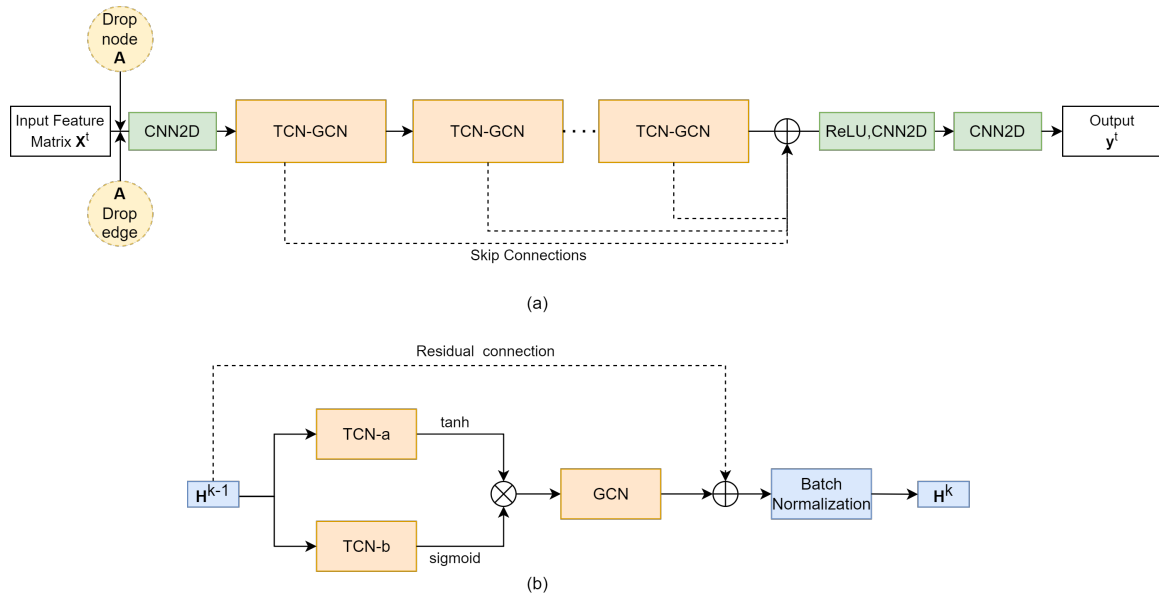


Figure 2. (a) GraphWavenet used in this work consists of a number of temporal convolution network and graph convolution network (TCN-GCN) modules for progressively encoding input data \mathbf{X}^t ; the outputs of each TCN-GCN are skip-connected to improve learning; 1×1 kernel convolutional neural network (CNN) layers are used as linear transformation layers; optionally, nodes and edges in the adjacency matrix \mathbf{A} are randomly masked for improving training and for graph coarsening (i.e., DropNode and DropEdge); (b) the internal design of each TCN-GCN module, which consists of interleaved TCN and GCN layers to process information from one hidden layer to the next. The layer input and output are connected via residual connections to improve training.

240 In general, the graph-based learning seeks to learn a low-dimensional representation of input data through recurrent information aggregation and propagation steps. At the node level, a basic GNN layer may be written as (Bronstein et al., 2021)

$$\mathbf{h}_v^{(k)} = f \left(\mathbf{h}_v^{(k-1)}, \bigoplus_{u \in \mathcal{N}_v} (\psi(\mathbf{h}_u, \mathbf{h}_v)) \right), \quad (1)$$

245 where $\mathbf{h}_v^{(k)} \in \mathbb{R}^{D_k}$ denotes the embedding or hidden state of node v at the k -th layer, D_k is the output dimension of the k -th hidden layer and $\mathbf{h}_v^{(0)} = \mathbf{x}_v$; \bigoplus is an aggregation operator; ψ is a learnable function parameterizing the messaging passing between node v and its neighbors $u \in \mathcal{N}_v$; and $f(\cdot)$ is an activation function (e.g., the Rectified



Linear Unit function or ReLU). Most GNNs differ by how \oplus and ψ are chosen. For example, in the GCN layer that is used within GWN, the following aggregation scheme is used, (Kipf and Welling, 2016)

$$\mathbf{h}_v^{(k)} = f \left(\mathbf{W}_1^{(k)} \mathbf{h}_v^{(k-1)} + \mathbf{W}_2^{(k)} \sum_{u \in \mathcal{N}_v} \mathbf{h}_u^{(k-1)} + \mathbf{b}^{(k)} \right), \quad (2)$$

250 where the weighted sum of the hidden states of neighboring nodes (2nd term in parentheses) is added to the node's embedding from the previous layer (1st term in parentheses). Here $\mathbf{W}_1^{(k)}$ and $\mathbf{W}_2^{(k)}$, both $\in \mathbb{R}^{D_k \times D_{k-1}}$, are learnable weight matrices that determine the influences of node features and node neighbors, respectively; and \mathbf{b} is a learnable bias term added to improve training. At the graph level, the graph convolution operation in Eq. 2 may be written in a simplified matrix form as (Kipf and Welling, 2016)

$$255 \quad \mathbf{H}^{(k)} = f \left(\tilde{\mathbf{A}} \mathbf{H}^{(k-1)} \mathbf{W}^{(k)} \right), \quad (3)$$

where $\tilde{\mathbf{A}} = \mathbf{A} + \mathbf{I}$ is the adjacency matrix with self-loop (i.e., self-pointing links are added), \mathbf{I} is the identity matrix, $\mathbf{H}^{(k)} \in \mathbb{R}^{N \times D_k}$ includes all hidden-state node vectors in the k -th layer, and $\mathbf{W}^{(k)} \in \mathbb{R}^{D_{k-1} \times D_k}$ is a learnable weight matrix. In practice a normalized form of adjacency matrix is often used in lieu of Eq. 3 to improve numerical stability (Kipf and Welling, 2016),

$$260 \quad \hat{\mathbf{A}} = \tilde{\mathbf{D}}^{(-1/2)} \tilde{\mathbf{A}} \tilde{\mathbf{D}}^{(-1/2)}, \quad (4)$$

where $\tilde{\mathbf{D}}$ is a diagonal matrix containing the node degrees of $\tilde{\mathbf{A}}$.

For temporal learning, GWN adopts TCN, which uses a dilation factor to exponentially increase the receptive field of a CNN filter, thus allowing the capture of long-range dependencies using CNN (Wu et al., 2019; Zhang et al., 2020). Two TCNs (TCN-a and TCN-b in Fig. 2) are used in parallel to form a gated TCN block, as proposed by
 265 Dauphin et al. (2017),

$$\mathcal{X}^{(k)} = g(\Theta_1^{(k-1)} \mathcal{X}^{(k-1)} + \mathbf{b}_1^{(k-1)}) \odot \sigma(\Theta_2^{(k-1)} \mathcal{X}^{(k-1)} + \mathbf{b}_2^{(k-1)}), \quad (5)$$

where the $g(\cdot)$ function updates the hidden state using outputs from the previous layer $\mathcal{X}^{(k-1)} \in \mathbb{R}^{N \times D_{k-1} \times T_B}$, $\sigma(\cdot)$ is a gate function that regulates information flow from one layer to the next, Θ_i and \mathbf{b}_i are learnable weight matrices and bias terms, and \odot is the element-wise multiplication operator. In GWN, **tanh** is used for $g(\cdot)$ and
 270 **sigmoid** is chosen for $\sigma(\cdot)$. Multiple TCN-GCN modules are then stacked to learn spatial and temporal embeddings progressively. To improve ML learning, the input and output of each TCN-BCN module are connected for residual learning, and the outputs of all TCN-GCN modules are skip connected to the final output layer (see Fig. 2). Finally, 1×1 kernel CNN layers are used to condense the tensor dimensions and generate the desired outputs.

A well-known issue with the standard GNNs is oversmoothing, which happens when node-specific information is
 275 smoothed out after several rounds of message passing (Li et al., 2018). This can be especially problematic when



features from a node’s neighboring nodes become dominant, overshadowing the features of the node itself (Hamilton, 2020). Oversmoothing is a main reason behind the shallow design of many GNN. In the literature, two heuristic strategies have been proposed to mitigate oversmoothing, namely, node dropping and edge dropping. The former strategy randomly masks out a number of nodes in the adjacency matrix during each iteration of training, while
280 the latter strategy randomly drops a fraction of node edges. The DropEdge scheme, originally proposed by Rong et al. (2019), produces varying perturbations of the graph connections and, thus, can be seen as a data augmentation technique for training GNNs. In contrast, DropNode may be seen as both a training technique and a data imputation strategy—a GNN trained only on a subset of nodes can be used to predict nodes not seen during training. Previously, node masking was used for solving the Prediction at Ungauged Basins (PUB) problem (Sun et al., 2021). In this
285 work, we further demonstrated its use for solving the Prediction at Unmodeled Nodes (PUN) problem at the basin scale. We implemented both of these features as options within GWN (see Fig. 2).

As mentioned before, the GWN model is first trained using NWM outputs (pretraining) and then the network weights are fine-tuned using observation data. The fine-tuning step is often adopted in physics-guided ML studies to reduce biases of process-based models (Ham et al., 2019; Andersson et al., 2021).

290 3.2 Data fusion

After fine-tuning, the surrogate model may still be subject to errors resulting from ML approximations and from the process-based NWM. New observation data, when available, can be used to further reduce the surrogate model prediction error through a post-processing step. Our goal is closely related to that of the hydrologic post-processing, which seeks to establish a statistical relationship between model outputs and observations (Li et al., 2017). In
295 computer science, such post-processing is also related to label propagation, referring to assigning class labels to unclassified data using known data labels (Zhu and Ghahramani, 2002).

Let \mathbf{y} and $\hat{\mathbf{y}}$ denote the true and predicted values. In reality, \mathbf{y} can only be accessed at a limited number of observation nodes. Thus, \mathbf{y} is partitioned into two parts corresponding to observed (labeled) and unobserved (unlabeled) values, $\mathbf{y} \doteq [\mathbf{y}_L^T, \mathbf{y}_U^T]^T$. Further, assume \mathbf{y} is multi-Gaussian, $\mathbf{y} \sim \mathcal{N}(\boldsymbol{\mu}, \boldsymbol{\Sigma})$, with mean $\boldsymbol{\mu}$ and covariance matrix $\boldsymbol{\Sigma}$.
300 Streamflow values, which typically follow non-Gaussian distributions, can be projected into the normal space via a normal transform technique (Li et al., 2017). As a matter of fact, this normal transform generally improves ML training and, thus, should be done as part of the data preprocessing before ML training starts.

The joint distribution of \mathbf{y} in terms of its subsets \mathbf{y}_L and \mathbf{y}_U may be written as (Bishop, 2006),

$$p(\mathbf{y}_L, \mathbf{y}_U) = \mathcal{N} \left(\begin{pmatrix} \boldsymbol{\mu}_L \\ \boldsymbol{\mu}_U \end{pmatrix}, \begin{pmatrix} \boldsymbol{\Sigma}_{LL} & \boldsymbol{\Sigma}_{LU} \\ \boldsymbol{\Sigma}_{UL} & \boldsymbol{\Sigma}_{UU} \end{pmatrix} \right). \quad (6)$$



305 It can be shown the conditional probability distribution of \mathbf{y}_U given \mathbf{y}_L , namely, $p(\mathbf{y}_U | \mathbf{y}_L)$, is also multi-Gaussian, for which the conditional mean $\boldsymbol{\mu}_{U|L}$ and covariance $\boldsymbol{\Sigma}_{U|L}$ are (Bishop, 2006)

$$\begin{aligned}\boldsymbol{\mu}_{U|L} &= \boldsymbol{\mu}_U + \boldsymbol{\Sigma}_{UL}\boldsymbol{\Sigma}_{LL}^{-1}(\mathbf{y}_L - \boldsymbol{\mu}_L) = \boldsymbol{\mu}_U - \boldsymbol{\Gamma}_{UU}^{-1}\boldsymbol{\Gamma}_{UL}(\mathbf{y}_L - \boldsymbol{\mu}_L), \\ \boldsymbol{\Sigma}_{U|L} &= \boldsymbol{\Sigma}_{UU} - \boldsymbol{\Sigma}_{UL}\boldsymbol{\Sigma}_{LL}^{-1}\boldsymbol{\Sigma}_{LU} = \boldsymbol{\Gamma}_{UU}^{-1},\end{aligned}\quad (7)$$

where $\boldsymbol{\Gamma}$, known as the precision matrix, is the inverse of the covariance matrix. In the regression problem considered here, $\boldsymbol{\mu}_U$ may represent the ML estimates at unobserved locations, $\hat{\mathbf{y}}_U$, and \mathbf{y}_L may represent gage observations, then Eq. 7 forms the basis of updating the ML predictions $\hat{\mathbf{y}}_U$ through observations \mathbf{y}_L . To adapt the residual propagation for GNNs, Jia and Benson (2020) proposed the following parameterization of the precision matrix,

$$\boldsymbol{\Gamma} = \beta(\mathbf{I} - \alpha\mathbf{S}), \quad (8)$$

where $\mathbf{S} = \mathbf{D}^{-1/2}\mathbf{A}\mathbf{D}^{1/2}$ is similar to the normalized adjacency matrix defined in Eq. 4 but with self-loops removed; β and α are learnable shape parameters, the former controls the residual magnitude and the latter reflects the correlation structure. Later, the same authors proposed a residual propagation form involving a single hyperparameter ω (Jia and Benson, 2021),

$$\hat{\mathbf{y}}_{U|L} = \hat{\mathbf{y}}_U - (\mathbf{I} + \omega\mathbf{N})_{UU}^{-1}(\mathbf{I} + \omega\mathbf{N})_{UL}\mathbf{r}, \quad \mathbf{r} \doteq (\mathbf{y}_L - \hat{\mathbf{y}}_L) \quad \text{and} \quad \mathbf{N} \doteq \mathbf{I} - \mathbf{S} \quad (9)$$

where the labeled and unlabeled parts of $\mathbf{I} + \omega\mathbf{N}$ are extracted by using mask matrices, \mathbf{r} is defined as the residual vector between observations and ML predictions. Eq. 9 is the form of data fusion used in this study, which is model agnostic. The hyperparameter ω may be obtained by cross validation. The only time-varying part in Eq. 9 is \mathbf{r} and other matrix terms can be calculated offline, thus the update can be applied efficiently in real time.

We remark that the conditional mean and covariance shown in Eq. 7 are generally related to the Gaussian Process regression (Rasmussen and Williams, 2006) and has been used in the hydrologic post-processing literature, for example, in the General Linear Model Post-Processor in (Ye et al., 2014). However, the main difference is the data fusion is extended to operate on graphs via Eq. 9. An advantage of the residual propagation approach taken here is that it allows consideration of spatial correlation among node prediction errors while respecting the graph topology. Intuitively, we expect that unobserved nodes adjacent to a gauged node should share similar spatial and temporal patterns. The data fusion approach adopted here is different from the data assimilation method in (Jia et al., 2021), in which a prediction is made by using the features of a node and its neighboring nodes, but not directly considering predictions of the neighboring nodes, thus limiting the use of spatial information (Jia and Benson, 2020).

4 Study Area and Experiment Design

4.1 Description of the study area

The algorithms and workflow described in Section 3 are generic. For demonstration purposes, we consider the East-Taylor Watershed (ETW), a HUC-8 watershed (drainage area 1984.7 km²) that lies within the Gunnison River



335 basin (HUC-4) in the southern Rocky Mountains of Colorado, U.S. (Fig. 3). The ETW is representative of the
high-altitude river basins in the upper Colorado River basin. Elevation of the watershed ranges approximately from
2,440 to 4,335 m (McKay et al., 2012). Climate of the watershed is defined as continental, subarctic climate with
long, cold winters and short, cool summers (Hubbard et al., 2018). Annual precipitation ranges from 1350 mm/yr
340 of precipitation falls as snow (see Fig. S1a in Supporting Information (SI)); annual temperature is in the range of -3
to 1 °C in the area (Fig. S1b) (PRISM Climate Group, 2022).

The ETW encompasses two alpine rivers, the East River in the west and the Taylor River in the east, both flowing
into the Gunnison River in the south which, in turn, serves as a main tributary of the Colorado River, contributing
about 40 percent of its streamflow (Battaglin et al., 2011). The East River watershed is mostly undeveloped, other
345 than the city of Crested Butte (population 1339) and the ski resort area that are located near the middle course of
the river (Bryant et al., 2020). The Taylor River is dammed by Taylor Park Dam (storage capacity about 0.13 km³)
in the middle (Bureau of Reclamation, 2022).

Snowmelt provides the main source of runoff in the watershed, with peak discharge occurring between May
and July; baseflow conditions prevail from August until the winter freeze (Bryant et al., 2020). Like many other
350 snow-dominated systems in the western U.S., streamflow pattern in the ETW is influenced by frequent droughts
and heatwaves in recent years (Winnick et al., 2017), and is likely to undergo further changes with the projected
lower snowfall and earlier snowmelt under future climate conditions (Davenport et al., 2020). Globally, tremendous
interests exist in the hydroclimate modeling community to understand and predict streamflows in snow-dominated
regions under global environment change (Barnett et al., 2005; Qin et al., 2020).

355 Five USGS gages in the watershed are identified to have continuous records (open circles in Fig. 3) and are used
as the source for fine-tuning and data fusion in this work. Notably Gage 09107000 and Gage 09109000 are located
immediately upstream and downstream of the Taylor Park Dam. The mean annual flow at the outlet of East River
(Gage 09112500) is 9.3 m³/s, and at the outlet of Taylor River (Gage 09110000) it is 9.2 m³/s, both are estimated
based on 110 years of data from 1911–2021 (USGS, 2022a). An extra USGS gage (red circle) with incomplete record
360 is also identified for validation purposes.

The ETW contains 23 subbasins (dark lines in Fig. 3) at the HUC-12 level and a total of 552 NHDPlus flowlines or
reaches (dark blue polylines in Fig. 3). The NHDPlus reach lengths range from 0.047 to 11.48 km, the stream order
ranges from one (the headwater tributaries) to five (Taylor River downstream of the reservoir), and the drainage
area of reaches ranges from 0.027–24.99 km². Thus, ETW presents an interesting study area from the perspective
365 of river network modeling: it encompasses two contrasting flow regimes, the East River that is under natural flow
conditions and the Taylor River that is subject to human intervention; it also includes a meaningful degree of spatial
heterogeneity that is representative of a snow-dominated, mountainous watershed.

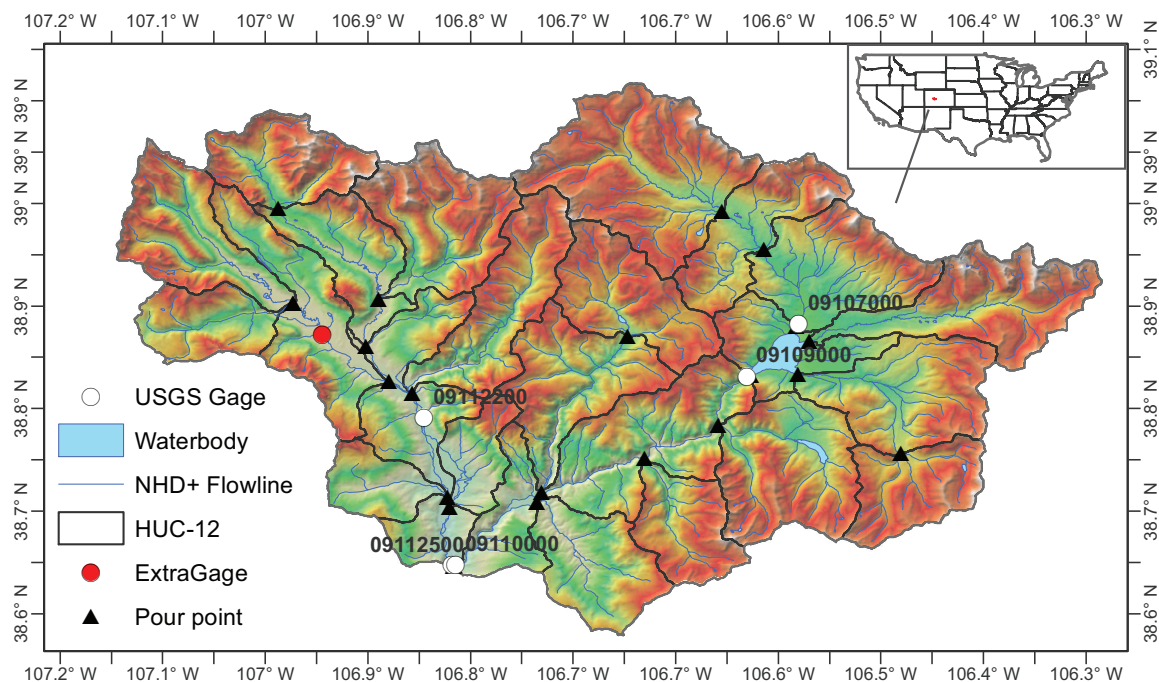


Figure 3. Shaded relief map of the East-Taylor watershed (HUC-8 code 14020001), overlaid by the NHDPlus flowline (solid blue lines), five USGS gage locations (open circles) used for fine-tuning and data fusion, the HUC-12 subbasin boundaries (solid dark lines) and pour points (triangles), and the surface waterbody (light blue) layer. An extra gage (red circle) is held for additional validation

4.2 Experimental design and model training

We performed a series of ML experiments to address the two objectives of this study, namely, evaluating the role of physical realism in river network representation and the efficacy of graph-based data fusion. The study period is set to 1993/01–2018/12, the same as the NWM v2.0’s retrospective simulation period. All scripts are written in Python and, in particular, PyTorch (Paszke et al., 2019) is used to develop all GNN and data fusion codes. The open-source GWN code (Wu et al., 2019) and GNN data fusion code (Jia and Benson, 2020) are adapted for the problem at hand. The train/validation/testing split used is (0.7, 0.15, 0.15). Streamflow data is projected to normal space by using a power transformer scaler proposed in (Yeo and Johnson, 2000) and available from `scikit-learn` (Pedregosa et al., 2011), in which the scaler is first fit to the training data and then applied to the remainder of the dataset. An inverse transform is then applied at the end to convert the results back to the original space.

The node-based ETW river network is constructed based on the NHDPlus flowlines and associated reach IDs (COMIDs) by following the procedures described under Section 2.3. A cutoff threshold is applied to extract a subset of river reaches. Thresholding is a common practice in climate networks to help reveal dominant spatiotemporal structures (Donges et al., 2009a, b; Malik et al., 2012). Here all reaches with a medium flow value less than 0.01



m^3/s (approximately at the 30th percentile of median flow distribution of all nodes) are trimmed from the network, keeping 295 out of a total of 552 nodes. In the resulting adjacency matrix, two nodes are connected if an NHDPlus flowline of “streamriver” type exists between them. Reaches falling on the water bodies (light blue polygons in Fig. 3) are not included in the river network. We used undirected and unweighted adjacency matrices. As an ablation study, we also considered NWM v2.1 data, which resulted in a 348-node network after trimming. The different numbers of node probably reflect differences in model parameterization and forcing data between the two NWM versions (see Section 2). The HUC-12 subbasin-based ETW river network is constructed by using the information in the NHDPlus pour point layer (Price, 2022) for connecting each subbasin to its neighbors.

Unless otherwise noted, we train the model with a lookback period of 30 days, which is sufficient for the current case when simulated antecedent flows are also used as predictors to drive streamflow predictions. The forecast horizon is one-day ahead. The number of TCN-GCN blocks used is 7, the kernel used in TCN layers is 1×4 , the number of filters used in dilation and residual blocks are both 32. We use AdamW, a modified version of the Adam gradient-based optimizer, for training the network (Loshchilov and Hutter, 2018). The mini-batch size is 30.

When using the DropEdge option, we randomly enable 80 percent of the edges in the adjacency matrix at the beginning of each epoch. This is done by flattening the adjacency matrix into a vector, performing random permutation, and taking the first 80 percent of connection. When the DropNode option is on, we use a mask matrix to mask the indices of nodes to be dropped. The training parameter selection is largely based on our previous experience (Sun et al., 2021). For each GWN configuration, 10 different models are trained by initializing with different random seeds. For pretraining, the loss function used is the mean absolute error (MAE) or L_1 norm between ML predictions and NWM outputs, while for fine-tuning, the loss function is the L_1 norm between ML predictions and observed streamflow at the five gage locations. Pretraining is done for 60 epochs with a learning rate of 0.0005. Starting with the weights of a pretrained model, fine-tuning is done for another 15 epochs but with a smaller learning rate of $1e - 5$. Training time is around 1.3 min wallclock time per epoch for the 295-node models, and 14 sec per epoch for the 23-node models, on the same Nvidia V100 GPU.

We quantify the performance of trained models on test data using three metrics, namely, normalized root mean square error (NRMSE), Kling–Gupta efficiency (KGE) (Gupta et al., 2009), and Pearson’s correlation (R). Definitions of the metrics and L_1 norm are given in the Appendix. The hyperparameter ω in Eq. 9 is selected through leave-one-out cross validation (LOOCV). Specifically, the ω value is varied in the range (50, 5000) with a step size of 50. For each ω , we perform LOOCV by using four of the five gages for residual propagation, and calculating the MAE on the holdout gage. The ω that gives the minimum mean MAE across all gages is selected for data fusion.



5 Results

5.1 Pretraining

We first demonstrate the efficacy of GWN and its variants for approximating the NWM (i.e., the pretraining stage).
415 Three sets of GWN models are trained. The first set uses the original GWN configuration with the self-loop adjacency
matrix $\tilde{\mathbf{A}}$ (defined in Eq. 3) corresponding to the actual ETW network (GWN-O), the second set uses the same
 $\tilde{\mathbf{A}}$ as input but is trained by activating the DropEdge feature to randomly remove node links (GWN-DropEdge),
and the third set is trained using only a subset of nodes in $\tilde{\mathbf{A}}$ (GWN-Impute). Thus, physical realism is gradually
420 network containing 295 nodes, while the third set uses the HUC-12 pour point set as nodes (see Fig. 3).

Table 1 summarizes the performance metrics of all three models in KGE, NRMSE, and R. Results suggest the
GWN-O achieves high scores under all three metrics. GWN-DropEdge gives almost the same performance. GWN-
Impute, which is trained using less than one-tenth of the nodes used in the other two models, also achieves a
reasonable performance. Fig. 4 shows the empirical cumulative distribution function (ECDF) and node-level maps
425 of KGE and NRMSE that are obtained by the GWN-O surrogate model. The KGE is close to 1.0 (NRMSE close to
0.0) on the mainstems of East and Taylor rivers, but drops (increases) slightly in several tributaries of the Taylor
River in the middle and southeast part of the watershed. Performance at subbasins disconnected by the Taylor
Park Dam does not appear to be strongly affected. All reaches adjacent to the reservoir show high KGE. This is
interesting, suggesting the antecedent NWM outputs provide sufficient node-level information for the GNN to learn.

430 As an ablation study, we trained a GWN-O model using only Daymet forcing data while keeping all other config-
urations unchanged. Results, shown in Fig. S2 of the SI, suggest the performance of the data-driven surrogate model
is deteriorated, especially in the mid-range of both rivers. One possible explanation is without using the antecedent
NWM outputs as predictors, the data-driven models may either require a much longer lookback period to achieve
meaningful results (Kratzert et al., 2019a), or simply cannot explain all variations in the NWM outputs. The latter
435 reason points to the inherent difficulty in learning the data-driven, input-output mapping in this snow-dominated
watershed. Previously, Ma et al. (2017) evaluated the performance of NOAA-MP, which is the land model in WRF-
Hydro, in modeling the snow cover function (SCF). By definition, SCF is the fraction of a grid cell covered by snow,
and provides an indirect measure of snow mass and snow depth. They found that the modeled SCF agrees well with
the gridded SCF product derived from Moderate Resolution Imaging Spectroradiometer (MODIS), with relative
440 biases varying from 4% in the snow accumulation phase to 14% in the melting phase. The authors attributed the
good performance to the SCF scheme, the use of a vegetation canopy snow interception module, and the multilayer
snowpack representation implemented in NOAA-MP (Ma et al., 2017). Thus, these sophisticated parameter schemes
in NWM may not be explained by using Daymet forcing alone.

We compare the KGE between GWN-O and the other two models in Fig. 5. The performances of GWN-O and
445 GWN-DropEdge are similar, only slight KGE differences are noted in the headwater tributaries of Taylor River,



indicating the GWN models are relatively robust to perturbations induced through dropping edges. This is again because the same NWM data is behind GWN-O and GWN-DropEdge and strong auto-correlation exists at the node level. Between GWN-O and GWN-Impute, GWN-O outperforms in the headwater subbasins. Nevertheless, the accuracy of GWN-Impute is high on the mainstems.

Table 1. Performance metrics of pretrained GraphWaveNet (GWN) surrogate models. GWN-O is the original model of Wu et al. (2019), GWN-DropEdge implements random edge sampling, GWN-Impute is trained on a subset of 23 nodes corresponding to the HUC-12 pour points. All results reported are based on ensemble averages from 10 models trained with different random seeds.

Model	Median	Mean	Max	Min
KGE, range $(-\infty, 1]$				
GWN-O	0.978	0.947	0.998	0.574
GWN-DropEdge	0.978	0.947	0.998	0.584
GWN-Impute	0.975	0.915	0.997	0.445
NRMSE, range $[0, \infty)$				
GWN-O	0.188	0.256	1.126	0.021
GWN-DropEdge	0.186	0.262	1.132	0.023
GWN-Impute	0.214	0.300	1.455	0.039
R, range $[-1, 1]$				
GWN-O	0.991	0.985	1.000	0.877
GWN-DropEdge	0.990	0.984	1.000	0.912
GWN-Impute	0.990	0.982	0.999	0.906

450 To elucidate why GWN-Impute gives a good performance on ETW, we plot the node correlation heatmap in Fig. 6. Subbasins 1–13 are on the Taylor River side, while subbasins 14–23 are on the East River side of the ETW (Fig. 6a). An immediate observation is the block structure along the diagonal of heatmap in Fig. 6c, suggesting inside each subbasin strong cross-node correlations exist. Specifically, subbasin 13, the most downstream basin on the Taylor River side, exhibits the highest inner-basin correlation, while the upstream headwaters basins (subbasins 1 and 2) show more inner-basin variations. Subbasin 13 also shows relatively strong cross-basin correlations with other subbasins on both the East River and Taylor River sides. This is because subbasin 13 is at the confluence of the two rivers, thus reflecting information passed from the upstream of both rivers. Similarly, the downstream basins on the East River side, namely, subbasins 22 and 23, also show relatively strong inter-basin correlations with other basins on the East River side. In contrast, isolated remote subbasins (e.g., #14 on East River side, and #1 and #11 on Taylor River side as labeled below Fig. 6c) do not exhibit strong inter-basin correlations. These observations are further corroborated using the graph betweenness centrality, defined as the number of shortest paths that pass through a

455

460

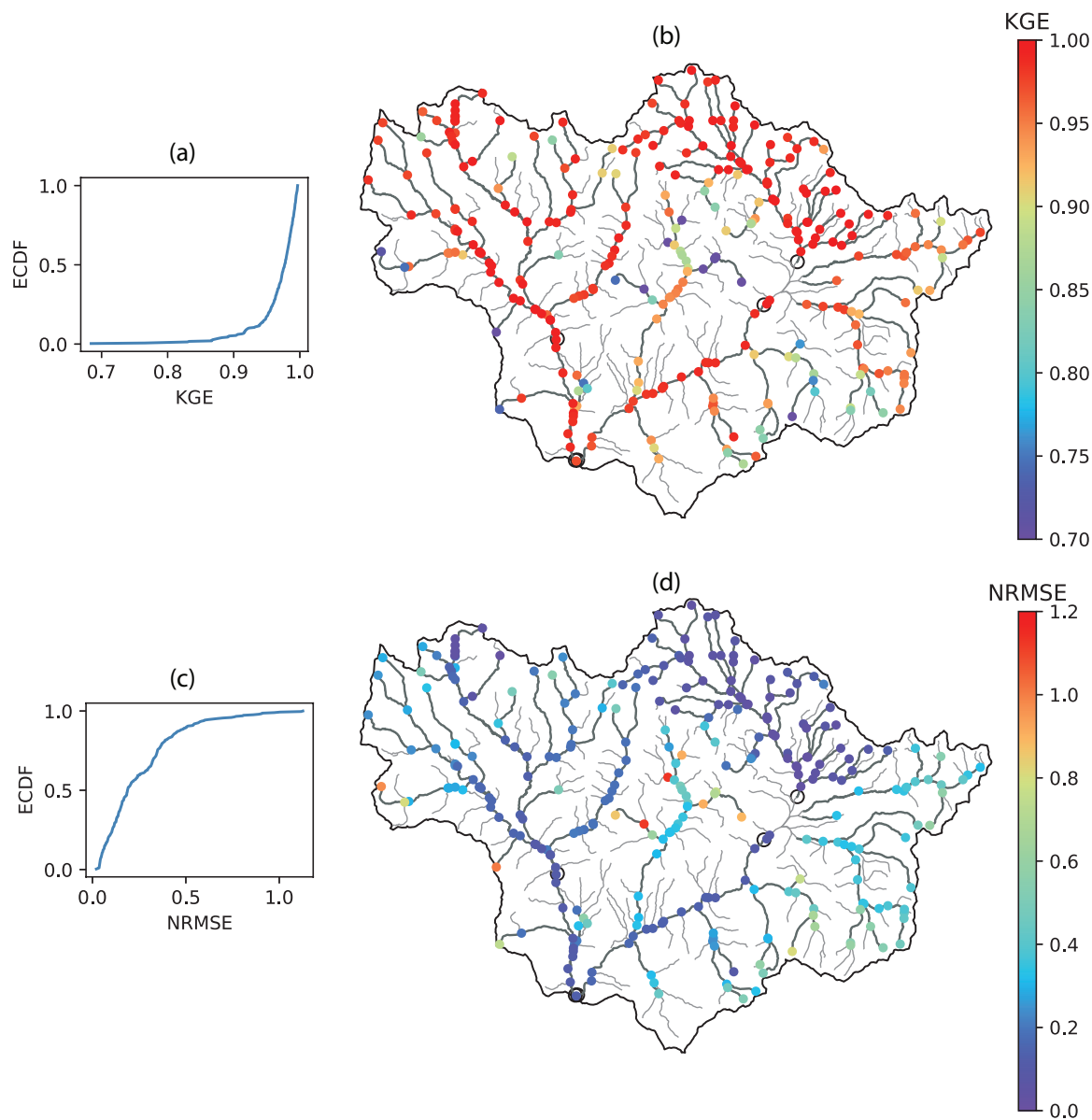


Figure 4. Test performance metrics obtained using the pretrained 295-node GraphWaveNet (GWN-O) model. (a)&(b) empirical cumulative distribution function (ECDF) and node map of KGE; (c)&(d) ECDF and node map of NRMSE. Results are obtained based on the ensemble mean of a 10-member ensemble. Gage locations are shown as open circles on node maps.

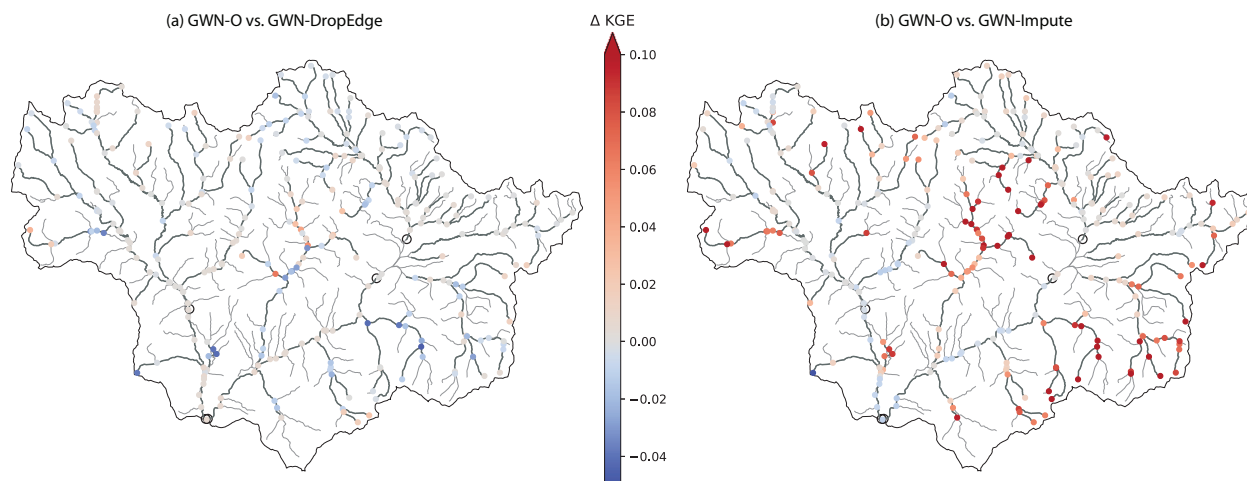


Figure 5. Node-level KGE comparison between the pretrained GWN-O and that of (a) GWN-DropEdge and (b) GWN-Impute.

node. Thus, nodes with a high betweenness centrality tend to have more influence on information propagation in the network (Donges et al., 2009b). Fig. 6b shows reaches in the downstreams of East and Taylor rivers have higher betweenness centrality values than the upstream nodes. The heatmap analysis reveals the model parameter structure and the degree of freedom of the underlying NWM which, in turn, determine how well the graph coarsening process may work. Essentially, in this case the pour-point based ML imputation is a physics-informed interpolation process. We expect the information content is richest at the pour point of each subbasin, thus a surrogate model trained using only pour-point information may sufficiently capture the dominant flow dynamics in the watershed and satisfactorily interpolate to all unmodeled points.

We conducted an ablation study using the 348-node network corresponding to NWM 2.1 (see also Section 4.2). Results are shown in Fig. S3. The newly added nodes are low-flow nodes appearing at the headwaters and small tributaries in subbasins. In this case, the median of the KGE is 0.974 and the mean is 0.937. Comparing to the model trained using NWM v2.0, the performance in subbasins #8, #10, #11 are significantly improved, however, the performance in headwater subbasins #1 and #2 on the Taylor River side also show some deterioration. This suggests the effect of model calibration between NWM versions may not be uniform across the model domain.

Experiments presented thus far provide useful insights on how much physical realism is needed when implementing GNNs for the purpose of river network surrogate modeling. It depends on the watershed hydroclimatic and physiographic attributes, the parameter structure of the underlying process-based model, and the objective of study. In the current case, we show that GWN models built on a coarsened graph give comparable performances as those built on more fine-grained representations of the river network, requiring only a fraction of training time. If the main objective of surrogate modeling is to capture the simulated streamflow patterns in the mainstem of a river (e.g., for

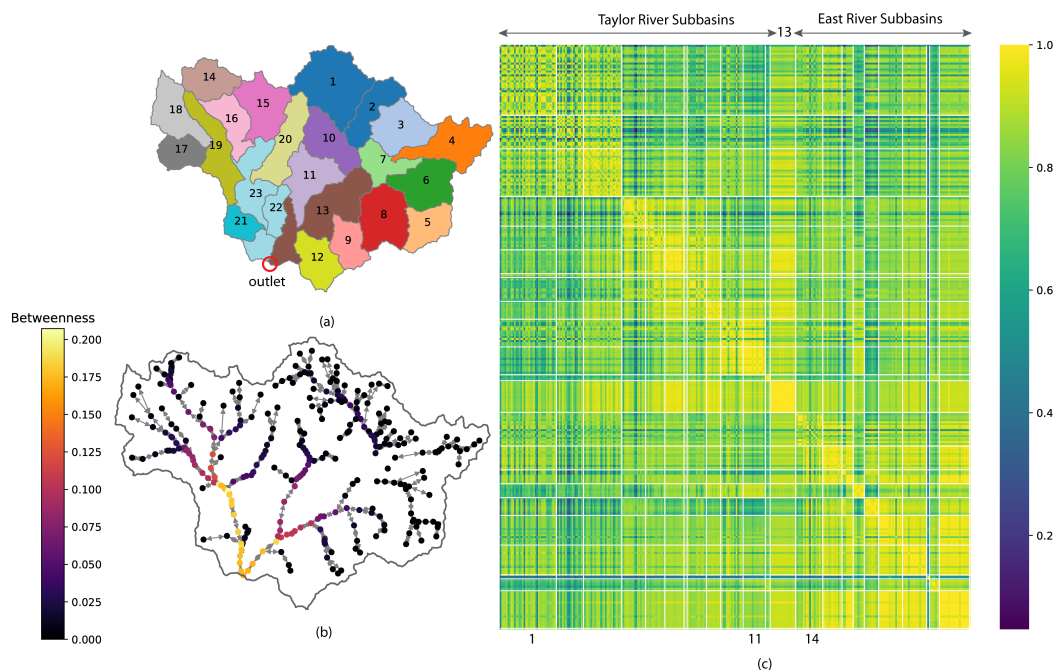


Figure 6. Node correlation heatmap generally exhibits a block structure within subbasins: (a) subbasin boundary map, where subbasins 1–13 are on the Taylor River side and subbasins 14–23 are on the East River side; (b) node correlation heatmap, where subbasin nodes are separately by white solid lines

estimating flood peaks), then all variants of the GWN models presented here should suffice. On the other hand, if the main objective is to simulate snowmelt and runoff in low-flow headwater basins, then more physical realism is required in the river network. These findings also shed light on scaling up the GNNs for modeling large river basins.

485 5.2 Fine-tuning

After pretraining, we fine-tune the GWN models by following the procedure described in Section 4.2. Table 2 reports the KGE and R of NWM, pretrained and fine-tuned GWN-O models against the five USGS gages (see Fig. 3 for their locations) over the testing period. The corresponding hydrographs are presented in Fig. 7. The KGE values of NWM simulations are relatively low, only Gage 09107000 (upstream of Taylor Park Dam) and Gage 09110000 (at pour
490 point Taylor River) have KGE values greater than 0.5. The pretrained GWN-O model reports similar KGE values as the NWM, which is by design. The fine-tuned GWN-O model, which is trained using the historical observations falling in the training period, improves the KGE values slightly over most gages, except for Gage 09112500 located in the mid-stream of East River. We also calculate the KGE values for winter season (NDJF months) and summer season (MJJA months) separately. The fine-tuned model captures the low flow on East River relative well (Gage



Table 2. Comparison of the KGE and R of NWM, pretrained GWN-O, fine-tuned GWO-O against the USGS gage data. The last four columns show the values for winter and summer seasons.

USGS Gage	KGE						
	NWM	GWN-O Pretrain	GWN-O Fine-tune	NWM (winter)	GWN-O Fine-tune (winter)	NWM (summer)	GWN-O Fine-tune (summer)
09107000	0.563	0.559	0.596	0.169	0.205	0.467	0.485
09112200	0.332	0.328	0.348	0.192	0.625	0.266	0.258
09112500	0.355	0.348	0.341	-0.076	0.741	0.289	0.248
09109000	0.425	0.425	0.624	-1.418	-0.146	0.323	0.524
09110000	0.616	0.610	0.665	-0.632	0.148	0.534	0.614
	R						
09107000	0.877	0.876	0.851	0.698	0.318	0.855	0.771
09112200	0.904	0.900	0.961	0.348	0.660	0.898	0.953
09112500	0.901	0.899	0.957	0.074	0.756	0.894	0.948
09109000	0.554	0.554	0.782	-0.471	-0.112	0.442	0.650
09110000	0.706	0.715	0.868	-0.337	0.195	0.618	0.788

495 09112200 and 09112500). However, all peak flows are underestimated, as can be seen from Fig. 7. In comparison, the fine-tuned model generally makes more improvement on R, except at Gage 09107000. The summer correlation values are higher than the winter values.

Overall, although fine-tuning of the GWN-O only leads to mild performance improvements in this case, the bias corrections, especially in the phase of the time series, are important for the subsequent data fusion step. In this work, we mainly utilized streamflow data, but other types of Earth observation data may also be integrated in the fine-tuning step to further improve model performance.

5.3 Data fusion

We investigate the efficacy of data fusion on the five USGS gages. The value of hyperparameter ω is determined according to the LOOCV procedure described under Section 4.2. For the fine-tuned 295-node GWN-O model, the optimal ω value is found to be 1500. Fig. 8 compares NWM v2.0, corrected GWN-O, and observed streamflow time series for the testing period, in which the KGE and correlation (R) between the corrected GWN-O and observations are shown in the subplot titles for each gage.

After data fusion, R becomes greater than 0.85 at all gage locations. In terms of KGE, the LOOCV data fusion has the greatest impact on Gage 09109000, achieving a value of 0.944. It also improves the two East River gages

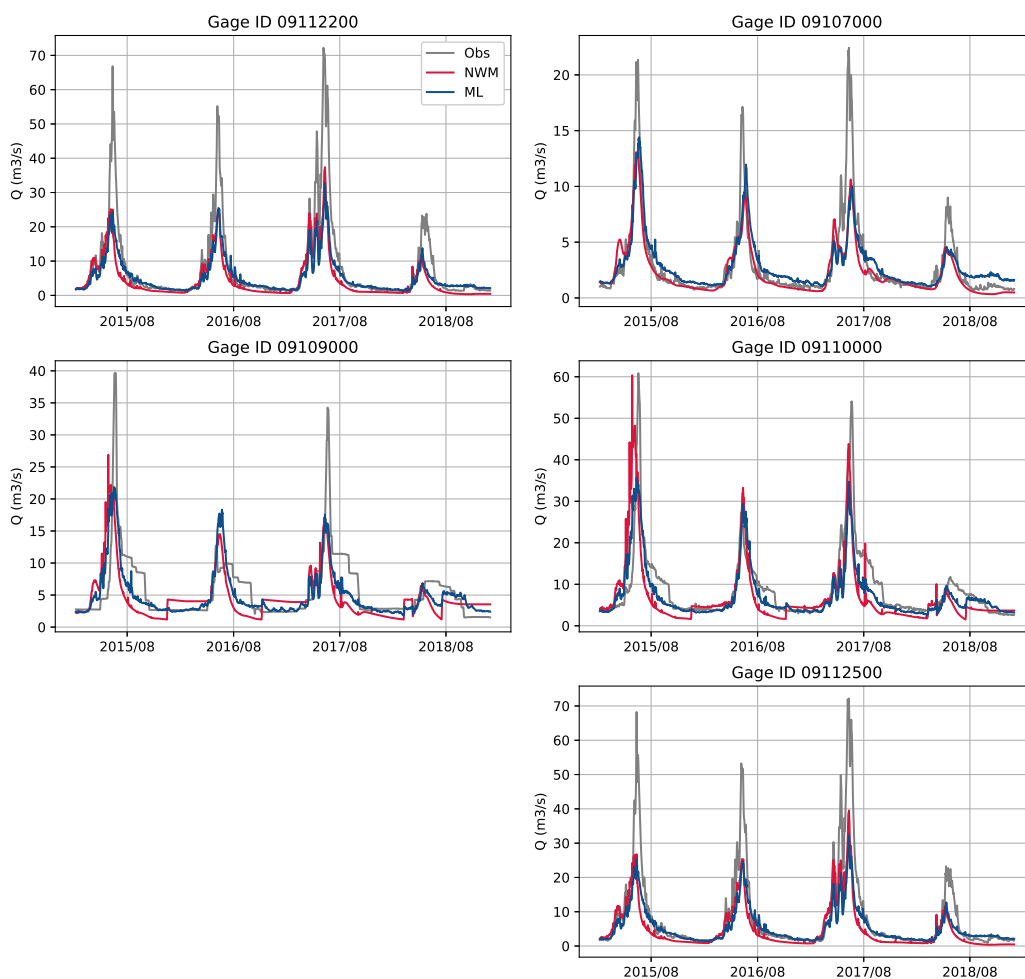


Figure 7. Hydrographs simulated by NWM (dark blue) and GWN-O (ML, dark red) vs. the USGS data (Obs, gray) over the testing period.



510 significantly (i.e., Gage 09112500 and 09112200). It has little effect on 09107000, which is upstream of the Taylor
Park Reservoir. It has a slightly negative impact on Gage 09110000, which is at the outlet of Taylor River. In
this case, Gage 091125000 and 09110000 are very close to each other (indirectly connected via the confluence node
between East and Taylor rivers), but reflecting different flow patterns. Specifically, Gage 09110000 is affected by
the reservoir releases, as can be seen from the zigzag pattern in Fig. 8, while Gage 091125000 is not subject to
515 such human intervention impact. The current data fusion scheme does not differentiate these different dynamics.
However, when all gages are used simultaneously in data fusion, we expect such interference to be reduced.

Fig. 9 shows the data fusion residual map, defined as the flow difference between data fusion and the NWM (i.e.,
 r in Eq. 9). The data fusion effect is greatest at the most downstream locations of both East and Taylor rivers and
then gradually fades out toward the upstream headwaters basins, reflecting the reduction in flow magnitudes when
520 traversing upstream, as well as the diminished influence of downstream gages.

The effect of data fusion effect is further validated using an extra USGS gage on East River, Gage 385106106571000,
that is not part of the model training and residual propagation (see Fig. 3 for its location). This is the only extra
gage in ETW that has a meaningful length of records (4475 days) for the study period. Results (Fig. 9) show that
data fusion significantly improved streamflow, increasing the KGE from 0.056 to 0.892.

525 As an ablation study, we applied the same data fusion procedure to another two models, the GWN-Impute model
and the GWN-O model trained without using NWM as predictors. The LOOCV results, shown in SI tables S1 and
S2, suggest that data fusion in general improves the results at most gage locations. The GWN-Impute model shows
comparable performance as the GWN-O model, although it is challenging for the GWN-O trained without using
NWM to yield good results. Thus, these results further demonstrate the robustness of a coarsened graph network
530 for modeling the study area.

6 Conclusions

GNNs, comprising nodes and edges and various constructs for graph-based information propagation, provide a
conceptually simple and yet powerful ML framework for learning vector hydrography. This work presents a multi-
stage, physics-guided ML framework that combines physics-based river network models with GNNs for streamflow
535 forecasting. In particular, our workflow, consisting of pretraining, fine-tuning, and data fusion stages, leverages
existing investment in high-performance river network models (e.g., the U.S. National Water Model) and Earth
observation data.

We demonstrated the merits of the GNN-based framework over the East Taylor watershed, a snow-dominated
system located in the Upper Colorado river basin. The watershed, which is representative of the snow-dominated
540 river basins in the western U.S., presents meaningful challenges from both the scientific and ML perspectives. On
the science side, significant research interests exist in understanding and predicting snowpack depth and shift in
snowmelt timing under projected climate change. On the ML side, challenges remain on scaling graphs for solving

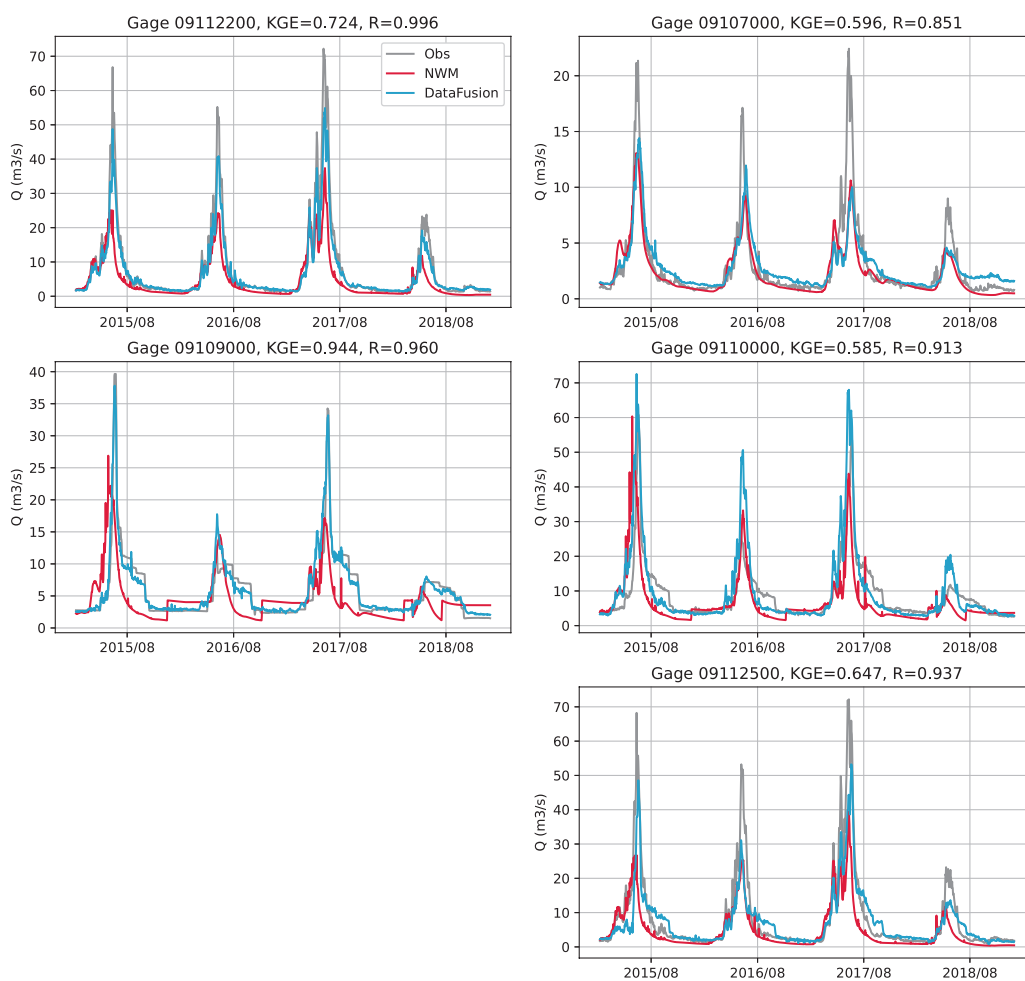


Figure 8. Hydrographs simulated by NWM (dark red) and corrected GWN-O (Data Fusion, lightblue) vs. the USGS data (Obs, gray) over the testing period. KGE and R shown in the subplot titles are calculated between data fusion and observations.

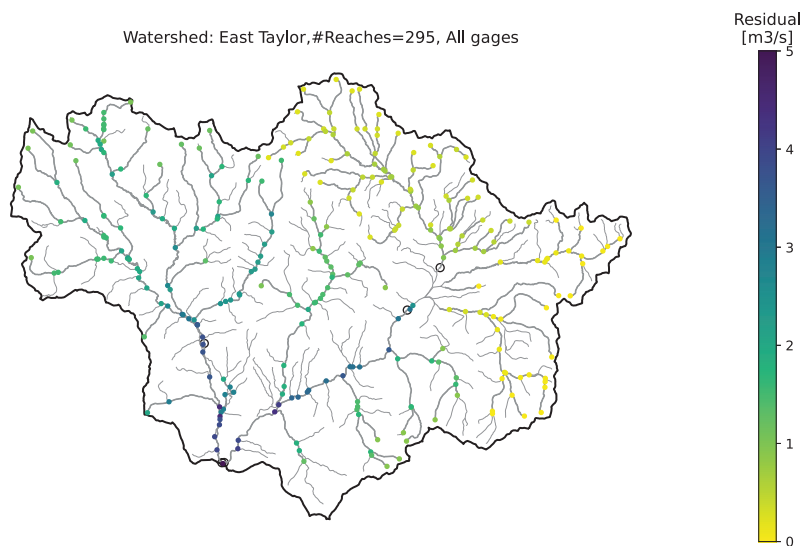


Figure 9. Residuals resulting from the data fusion using all five USGS gages. The greatest correction effect is seen at the downstream points.

large-scale graph-based regression problems. We showed that graph coarsening offers a feasible solution by exploiting the parameter structure of the underlying physics-based model. Thus, the designs of GNN and physics-based models can be asymmetric. When the physics-based model is already fine grained, which is the case in our work, the number of nodes in the GNN models can be significantly reduced. This same idea can be further expanded to embrace multiscale and/or multi-fidelity modeling to address different study objectives, such as coupling a fine-mesh network for biogeochemical transport with a coarse-mesh network for streamflow modeling. Heterogeneous graphs may be adopted for those applications (Wang et al., 2019). Finally, we show that graph-based data fusion provides a powerful post-processing tool for “nudging” streamflow observations, allowing error residuals to traverse over the entire network. Thus, this study, although demonstrated over a single watershed, lays the ground for future large-scale river basin analyses.

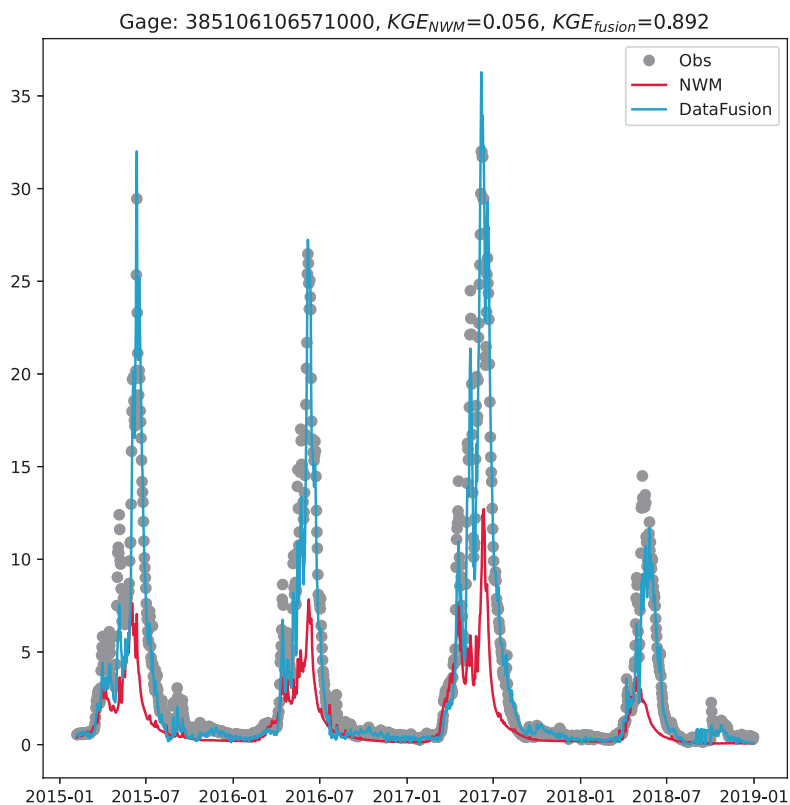


Figure 10. The effect of data fusion is validated on Gage 385106106571000 which is not used in any ML training and residual propagation. The KGE is improved from 0.056 to 0.892.

Code and data availability. We adapted the open-source GraphWavenet code <https://github.com/nanzhan/Graph-WaveNet>, data fusion code <https://github.com/000Justin000/gnn-residual-correlation>, and DropEdge [https://github.com/DropEdge/](https://github.com/DropEdge/DropEdge/) DropEdge in this work. The graph betweenness is generated using NetworkX <https://networkx.org>.

NWM retrospective simulation (v2.0 and v2.1) data can be downloaded from AWS (<https://registry.opendata.aws/nwm-archive>). Alternatively, NWM data (v2.0) can be downloaded from Hydroshare (<https://www.hydroshare.org>). Daymet data can be downloaded from <https://daymet.ornl.gov/>. NHDPlus database can be downloaded from EPA's NHDPlus site, <https://www.epa.gov/waterdata/get-nhdplus-national-hydrography-dataset-plus-data>.



560 Appendix A: Definition of performance metrics

The performance metrics used in this work are defined as

$$\text{NRMSE} = \frac{1}{\bar{Q}_{obs}} \sqrt{\frac{\sum_{t=1}^n (Q_{obs}^t - Q_{sim}^t)^2}{n}} \quad (\text{A1})$$

$$\text{R} = \frac{\sum ((Q_{sim}^t - \bar{Q}_{sim})(Q_{obs}^t - \bar{Q}_{obs}))}{\sqrt{\sum_{t=1}^n (Q_{sim}^t - \bar{Q}_{sim})^2 \sum_{t=1}^n (Q_{obs}^t - \bar{Q}_{obs})^2}} \quad (\text{A2})$$

565

$$\text{KGE} = 1 - \sqrt{(1 - \text{R})^2 + (1 - \mu_{sim}/\mu_{obs})^2 + (1 - \sigma_{sim}/\sigma_{obs})^2} \quad (\text{A3})$$

$$\text{MAE} = \frac{1}{n} \sum_{t=1}^n |Q_{obs}^t - Q_{sim}^t| \quad (\text{A4})$$

where Q_{obs} and Q_{sim} are observed and predicted values, respectively, \bar{Q} denotes the mean values, and n is the total
570 number of test data. The KGE score combines the linear Pearson correlation (R), the bias ratio μ_{sim}/μ_{obs} , and
the variability ratio $\sigma_{sim}/\sigma_{obs}$ (Gupta et al., 2009). The range of KGE is $(-\infty, 1]$. A KGE value greater than -0.41
indicates the model improves upon the mean flow (Knoben et al., 2019). The range of NRMSE is $[0, \infty)$. The mean
absolute error (MAE), or L_1 norm, quantifies the absolute difference between simulated and measured values.

Author contributions. A.Sun was responsible for the conceptualization, methodology, software, data curation, formal analysis,
575 and writing the original draft. P.Jiang, L.Yang, Y.Xie and X.Chen assisted with the conceptualization, review, and editing of
the paper.

Competing interests. The contact author has declared that neither they nor their co-authors have any competing interests.

Disclaimer. Publisher's note: Copernicus Publications remains neutral with regard to jurisdictional claims in published maps
and institutional affiliations.

580 *Acknowledgements.* This work was funded by the ExaSheds project, which was supported by the U.S. Department of Energy
(DOE), Office of Science, Office of Biological and Environmental Research, Earth and Environmental Systems Sciences



585 Division, Data Management Program. Pacific Northwest National Laboratory is operated for the DOE by Battelle Memorial Institute under contract DE-AC05-76RL01830. This paper describes objective technical results and analysis. Any subjective views or opinions that might be expressed in the paper do not necessarily represent the views of the U.S. Department of Energy or the United States Government. A. Sun wants to acknowledge the support of Texas Advanced Computing Center. A. Sun and Z.L. Yang are partly supported by DOE Advanced Scientific Computing Research under Grant DE-SC0022211.



References

- Alfieri, L., Burek, P., Dutra, E., Krzeminski, B., Muraro, D., Thielen, J., and Pappenberger, F.: GloFAS–global ensemble streamflow forecasting and flood early warning, *Hydrology and Earth System Sciences*, 17, 1161–1175, 2013.
- 590 Andersson, T. R., Hosking, J. S., Pérez-Ortiz, M., Paige, B., Elliott, A., Russell, C., Law, S., Jones, D. C., Wilkinson, J., Phillips, T., et al.: Seasonal Arctic sea ice forecasting with probabilistic deep learning, *Nature communications*, 12, 1–12, 2021.
- Barnett, T. P., Adam, J. C., and Lettenmaier, D. P.: Potential impacts of a warming climate on water availability in snow-dominated regions, *Nature*, 438, 303–309, 2005.
- 595 Battaglin, W. A., Hay, L. E., and Markstrom, S. L.: Watershed Scale Response to Climate Change–East River Basin, Colorado, US Geological Survey Fact Sheet, 3126, 2011.
- Bauer, P., Stevens, B., and Hazeleger, W.: A digital twin of Earth for the green transition, *Nature Climate Change*, 11, 80–83, 2021.
- Beck, H. E., De Roo, A., and van Dijk, A. I.: Global maps of streamflow characteristics based on observations from several
600 thousand catchments, *Journal of Hydrometeorology*, 16, 1478–1501, 2015.
- Best, J.: Anthropogenic stresses on the world’s big rivers, *Nature Geoscience*, 12, 7–21, 2019.
- Biancamaria, S., Lettenmaier, D. P., and Pavelsky, T. M.: The SWOT mission and its capabilities for land hydrology, in: *Remote sensing and water resources*, pp. 117–147, Springer, 2016.
- Bierkens, M. F., Bell, V. A., Burek, P., Chaney, N., Condon, L. E., David, C. H., de Roo, A., Döll, P., Drost, N., Famiglietti, J. S., et al.: Hyper-resolution global hydrological modelling: what is next? "Everywhere and locally relevant", *Hydrological processes*, 29, 310–320, 2015.
- 605 Bishop, C. M.: *Pattern recognition and machine learning*, Springer, 2006.
- Blöschl, G., Hall, J., Parajka, J., Perdigão, R. A., Merz, B., Arheimer, B., Aronica, G. T., Bilibashi, A., Bonacci, O., Borga, M., et al.: Changing climate shifts timing of European floods, *Science*, 357, 588–590, 2017.
- 610 Bronstein, M. M., Bruna, J., LeCun, Y., Szlam, A., and Vandergheynst, P.: Geometric deep learning: going beyond Euclidean data, *IEEE Signal Processing Magazine*, 34, 18–42, 2017.
- Bronstein, M. M., Bruna, J., Cohen, T., and Velicković, P.: Geometric deep learning: Grids, groups, graphs, geodesics, and gauges, *arXiv preprint arXiv:2104.13478*, 2021.
- Bruna, J., Zaremba, W., Szlam, A., and LeCun, Y.: Spectral networks and locally connected networks on graphs, *arXiv preprint arXiv:1312.6203*, 2013.
- 615 Bryant, S. R., Sawyer, A. H., Briggs, M. A., Saup, C. M., Nelson, A. R., Wilkins, M. J., Christensen, J. N., and Williams, K. H.: Seasonal manganese transport in the hyporheic zone of a snowmelt-dominated river (East River, Colorado, USA), *Hydrogeology Journal*, 28, 1323–1341, 2020.
- Bureau of Reclamation: Taylor Park Reservoir, <https://www.usbr.gov/projects/index.php?id=236>, 2022.
- 620 Camps-Valls, G., Tuia, D., Zhu, X. X., and Reichstein, M.: *Deep learning for the Earth Sciences: A comprehensive approach to remote sensing, climate science and geosciences*, John Wiley & Sons, 2021.



- Chen, S., Appling, A., Oliver, S., Corson-Dosch, H., Read, J., Sadler, J., Zwart, J., and Jia, X.: Heterogeneous stream-reservoir graph networks with data assimilation, in: 2021 IEEE International Conference on Data Mining (ICDM), pp. 1024–1029, IEEE, 2021.
- 625 Cosgrove, B., Gochis, D., Clark, E. P., Cui, Z., Dugger, A. L., Feng, X., Karsten, L. R., Khan, S., Kitzmiller, D., Lee, H. S., et al.: An overview of the National Weather Service national water model, in: AGU Fall Meeting Abstracts, vol. 2016, pp. H42B–05, 2016.
- Dai, A. and Trenberth, K. E.: Estimates of freshwater discharge from continents: Latitudinal and seasonal variations, *Journal of hydrometeorology*, 3, 660–687, 2002.
- 630 Dauphin, Y. N., Fan, A., Auli, M., and Grangier, D.: Language modeling with gated convolutional networks, in: International conference on machine learning, pp. 933–941, PMLR, 2017.
- Davenport, F. V., Herrera-Estrada, J. E., Burke, M., and Diffenbaugh, N. S.: Flood size increases nonlinearly across the western United States in response to lower snow-precipitation ratios, *Water Resources Research*, 56, e2019WR025 571, 2020.
- 635 David, C. H., Maidment, D. R., Niu, G.-Y., Yang, Z.-L., Habets, F., and Eijkhout, V.: River network routing on the NHDPlus dataset, *Journal of Hydrometeorology*, 12, 913–934, 2011.
- De Groot, R. S., Wilson, M. A., and Boumans, R. M.: A typology for the classification, description and valuation of ecosystem functions, goods and services, *Ecological economics*, 41, 393–408, 2002.
- Defferrard, M., Bresson, X., and Vandergheynst, P.: Convolutional neural networks on graphs with fast localized spectral
640 filtering, *Advances in Neural Information Processing Systems*, 29, 3844–3852, 2016.
- Döll, P., Kaspar, F., and Lehner, B.: A global hydrological model for deriving water availability indicators: model tuning and validation, *Journal of Hydrology*, 270, 105–134, 2003.
- Donges, J. F., Zou, Y., Marwan, N., and Kurths, J.: The backbone of the climate network, *EPL (Europhysics Letters)*, 87, 48 007, 2009a.
- 645 Donges, J. F., Zou, Y., Marwan, N., and Kurths, J.: Complex networks in climate dynamics, *The European Physical Journal Special Topics*, 174, 157–179, 2009b.
- Dottori, F., Szewczyk, W., Ciscar, J.-C., Zhao, F., Alfieri, L., Hirabayashi, Y., Bianchi, A., Mongelli, I., Frieler, K., Betts, R. A., et al.: Increased human and economic losses from river flooding with anthropogenic warming, *Nature Climate Change*, 8, 781–786, 2018.
- 650 EPA: National Hydrography Dataset Plus, <https://www.epa.gov/waterdata/get-nhdplus-national-hydrography-dataset-plus-data>, 2022.
- Feng, D., Fang, K., and Shen, C.: Enhancing streamflow forecast and extracting insights using long-short term memory networks with data integration at continental scales, *Water Resources Research*, 56, e2019WR026 793, 2020.
- Feng, D., Lawson, K., and Shen, C.: Mitigating prediction error of deep learning streamflow models in large data-sparse
655 regions with ensemble modeling and soft data, *Geophysical Research Letters*, 48, e2021GL092 999, 2021.
- Gochis, D., Barlage, M., Dugger, A., FitzGerald, K., Karsten, L., McAllister, M., McCreight, J., Mills, J., RafieeiNasab, A., Read, L., et al.: The WRF-Hydro modeling system technical description,(Version 5.0), NCAR Technical Note, 107, 2018.
- Grill, G., Lehner, B., Thieme, M., Geenen, B., Tickner, D., Antonelli, F., Babu, S., Borrelli, P., Cheng, L., Crochetiere, H., et al.: Mapping the world’s free-flowing rivers, *Nature*, 569, 215–221, 2019.



- 660 Gupta, H. V., Kling, H., Yilmaz, K. K., and Martinez, G. F.: Decomposition of the mean squared error and NSE performance
criteria: Implications for improving hydrological modelling, *Journal of hydrology*, 377, 80–91, 2009.
- Ham, Y.-G., Kim, J.-H., and Luo, J.-J.: Deep learning for multi-year ENSO forecasts, *Nature*, 573, 568–572, 2019.
- Hamilton, W. L.: Graph representation learning, *Synthesis Lectures on Artificial Intelligence and Machine Learning*, 14, 1–159,
2020.
- 665 Hamilton, W. L., Ying, Z., and Leskovec, J.: Inductive representation learning on large graphs, in: *Advances in Neural
Information Processing Systems*, pp. 1024–1034, 2017.
- Hochreiter, S. and Schmidhuber, J.: Long short-term memory, *Neural computation*, 9, 1735–1780, 1997.
- Hrachowitz, M., Savenije, H., Blöschl, G., McDonnell, J., Sivapalan, M., Pomeroy, J., Arheimer, B., Blume, T., Clark, M.,
Ehret, U., et al.: A decade of Predictions in Ungauged Basins (PUB)—a review, *Hydrological Sciences Journal*, 58, 1198–
670 1255, 2013.
- Hu, Z., Dong, Y., Wang, K., Chang, K.-W., and Sun, Y.: Gpt-GNN: Generative pre-training of graph neural networks, in:
Proceedings of the 26th ACM SIGKDD International Conference on Knowledge Discovery & Data Mining, pp. 1857–1867,
2020.
- Hubbard, S. S., Williams, K. H., Agarwal, D., Banfield, J., Beller, H., Bouskill, N., Brodie, E., Carroll, R., Dafflon, B.,
675 Dwivedi, D., et al.: The East River, Colorado, Watershed: A mountainous community testbed for improving predictive
understanding of multiscale hydrological–biogeochemical dynamics, *Vadose Zone Journal*, 17, 1–25, 2018.
- Jia, J. and Benson, A. R.: Residual correlation in graph neural network regression, in: *Proceedings of the 26th ACM SIGKDD
International Conference on Knowledge Discovery & Data Mining*, pp. 588–598, 2020.
- Jia, J. and Benson, A. R.: A unifying generative model for graph learning algorithms: Label propagation, graph convolutions,
680 and combinations, *arXiv preprint arXiv:2101.07730*, 2021.
- Jia, X., Zwart, J., Sadler, J., Appling, A., Oliver, S., Markstrom, S., Willard, J., Xu, S., Steinbach, M., Read, J., et al.:
Physics-guided recurrent graph model for predicting flow and temperature in river networks, in: *Proceedings of the 2021
SIAM International Conference on Data Mining (SDM)*, pp. 612–620, SIAM, 2021.
- Johnson, M. and Blodgett, D.: NOAA National Water Model Reanalysis Data at RENCI, *HydroShare*, [https://doi.org/10.
685 4211/hs.89b0952512dd4b378dc5be8d2093310f](https://doi.org/10.4211/hs.89b0952512dd4b378dc5be8d2093310f), 2020.
- Kashinath, K., Mustafa, M., Albert, A., Wu, J., Jiang, C., Esmailzadeh, S., Azizzadenesheli, K., Wang, R., Chattopadhyay,
A., Singh, A., et al.: Physics-informed machine learning: case studies for weather and climate modelling, *Philosophical
Transactions of the Royal Society A*, 379, 20200093, 2021.
- Kipf, T. N. and Welling, M.: Semi-supervised classification with graph convolutional networks, *arXiv preprint
690 arXiv:1609.02907*, 2016.
- Kitzmler, D. H., Wu, W., Zhang, Z., Patrick, N., and Tan, X.: The analysis of record for calibration: a high-resolution
precipitation and surface weather dataset for the united states, in: *AGU Fall Meeting Abstracts*, vol. 2018, pp. H41H–06,
2018.
- Knoben, W. J., Freer, J. E., and Woods, R. A.: Inherent benchmark or not? Comparing Nash–Sutcliffe and Kling–Gupta
695 efficiency scores, *Hydrology and Earth System Sciences*, 23, 4323–4331, 2019.
- Kratzert, F., Klotz, D., Herrnegger, M., Sampson, A. K., Hochreiter, S., and Nearing, G. S.: Toward improved predictions in
ungauged basins: Exploiting the power of machine learning, *Water Resources Research*, 55, 11 344–11 354, 2019a.



- Kratzert, F., Klotz, D., Shalev, G., Klambauer, G., Hochreiter, S., and Nearing, G.: Towards learning universal, regional, and local hydrological behaviors via machine learning applied to large-sample datasets, *Hydrology and Earth System Sciences*, 23, 5089–5110, 2019b.
- 700 Kratzert, F., Klotz, D., Hochreiter, S., and Nearing, G. S.: A note on leveraging synergy in multiple meteorological data sets with deep learning for rainfall–runoff modeling, *Hydrology and Earth System Sciences*, 25, 2685–2703, 2021.
- Le, X.-H., Nguyen, D.-H., Jung, S., Yeon, M., and Lee, G.: Comparison of deep learning techniques for river streamflow forecasting, *IEEE Access*, 9, 71 805–71 820, 2021.
- 705 Lehner, B. and Grill, G.: Global river hydrography and network routing: baseline data and new approaches to study the world’s large river systems, *Hydrological Processes*, 27, 2171–2186, 2013.
- Li, Q., Han, Z., and Wu, X.-M.: Deeper insights into graph convolutional networks for semi-supervised learning, in: *Proceedings of the AAAI Conference on Artificial Intelligence*, vol. 32, 2018.
- Li, W., Duan, Q., Miao, C., Ye, A., Gong, W., and Di, Z.: A review on statistical postprocessing methods for hydrometeorological ensemble forecasting, *Wiley Interdisciplinary Reviews: Water*, 4, e1246, 2017.
- 710 Lin, P., Yang, Z.-L., Gochis, D. J., Yu, W., Maidment, D. R., Somos-Valenzuela, M. A., and David, C. H.: Implementation of a vector-based river network routing scheme in the community WRF-Hydro modeling framework for flood discharge simulation, *Environmental Modelling & Software*, 107, 1–11, 2018.
- Lin, P., Pan, M., Beck, H. E., Yang, Y., Yamazaki, D., Frasson, R., David, C. H., Durand, M., Pavelsky, T. M., Allen, G. H., et al.: Global reconstruction of naturalized river flows at 2.94 million reaches, *Water resources research*, 55, 6499–6516, 2019.
- 715 Loshchilov, I. and Hutter, F.: Fixing weight decay regularization in adam, *arXiv preprint arXiv:1711.05101*, 2018.
- Lu, D., Konapala, G., Painter, S. L., Kao, S.-C., and Gangrade, S.: Streamflow simulation in data-scarce basins using Bayesian and physics-informed machine learning models, *Journal of Hydrometeorology*, 22, 1421–1438, 2021.
- 720 Ma, N., Niu, G.-Y., Xia, Y., Cai, X., Zhang, Y., Ma, Y., and Fang, Y.: A systematic evaluation of Noah-MP in simulating land-atmosphere energy, water, and carbon exchanges over the continental United States, *Journal of Geophysical Research: Atmospheres*, 122, 12–245, 2017.
- Malik, N., Bookhagen, B., Marwan, N., and Kurths, J.: Analysis of spatial and temporal extreme monsoonal rainfall over South Asia using complex networks, *Climate dynamics*, 39, 971–987, 2012.
- 725 McKay, L., Bondelid, T., Dewald, T., Johnston, J., Moore, R., and Rea, A.: *NHDPlus version 2: User guide*, US Environmental Protection Agency, 2012.
- Mizukami, N., Clark, M. P., Gharari, S., Kluzek, E., Pan, M., Lin, P., Beck, H. E., and Yamazaki, D.: A Vector-Based River Routing Model for Earth System Models: Parallelization and Global Applications, *Journal of Advances in Modeling Earth Systems*, 13, e2020MS002 434, 2021.
- 730 Moore, R. B. and Dewald, T. G.: The Road to NHDPlus–Advancements in Digital Stream Networks and Associated Catchments, *JAWRA Journal of the American Water Resources Association*, 52, 890–900, 2016.
- Newman, A., Clark, M., Sampson, K., Wood, A., Hay, L., Bock, A., Viger, R., Blodgett, D., Brekke, L., Arnold, J., et al.: Development of a large-sample watershed-scale hydrometeorological data set for the contiguous USA: data set characteristics and assessment of regional variability in hydrologic model performance, *Hydrology and Earth System Sciences*, 19, 209–223, 2015.
- 735



- NOAA: National Water Model CONUS Retrospective Dataset, <https://registry.opendata.aws/nwm-archive>, accessed Feb 15, 2022., 2022.
- Nonnenmacher, M. and Greenberg, D. S.: Deep emulators for differentiation, forecasting, and parametrization in Earth science simulators, *Journal of Advances in Modeling Earth Systems*, 13, e2021MS002554, 2021.
- 740 ORNL: Daymet web service, <https://daymet.ornl.gov>, 2022.
- Palmer, M. A., Reidy Liermann, C. A., Nilsson, C., Flörke, M., Alcamo, J., Lake, P. S., and Bond, N.: Climate change and the world's river basins: anticipating management options, *Frontiers in Ecology and the Environment*, 6, 81–89, 2008.
- Paszke, A., Gross, S., Massa, F., Lerer, A., Bradbury, J., Chanan, G., Killeen, T., Lin, Z., Gimelshein, N., Antiga, L., et al.: Pytorch: An imperative style, high-performance deep learning library, *Advances in neural information processing systems*, 745 32, 2019.
- Pathak, J., Subramanian, S., Harrington, P., Raja, S., Chattopadhyay, A., Mardani, M., Kurth, T., Hall, D., Li, Z., Aziz-zadenesheli, K., et al.: FourCastNet: A Global Data-driven High-resolution Weather Model using Adaptive Fourier Neural Operators, arXiv preprint arXiv:2202.11214, 2022.
- Pedregosa, F., Varoquaux, G., Gramfort, A., Michel, V., Thirion, B., Grisel, O., Blondel, M., Prettenhofer, P., Weiss, R., 750 Dubourg, V., Vanderplas, J., Passos, A., Cournapeau, D., Brucher, M., Perrot, M., and Duchesnay, E.: Scikit-learn: Machine Learning in Python, *Journal of Machine Learning Research*, 12, 2825–2830, 2011.
- Phillips, J. D., Schwanghart, W., and Heckmann, T.: Graph theory in the geosciences, *Earth-Science Reviews*, 143, 147–160, 2015.
- Pokhrel, Y., Hanasaki, N., Koirala, S., Cho, J., Yeh, P. J.-F., Kim, H., Kanae, S., and Oki, T.: Incorporating anthropogenic 755 water regulation modules into a land surface model, *Journal of Hydrometeorology*, 13, 255–269, 2012.
- Price, C.: WBD HU12 Pour Points derived from NHDPlus, <https://www.sciencebase.gov/catalog/item/5762b664e4b07657d19a71ea>, 2022.
- PRISM Climate Group: 30-year normals, <https://prism.oregonstate.edu/normals/>, 2022.
- Qin, Y., Abatzoglou, J. T., Siebert, S., Huning, L. S., AghaKouchak, A., Mankin, J. S., Hong, C., Tong, D., Davis, S. J., and 760 Mueller, N. D.: Agricultural risks from changing snowmelt, *Nature Climate Change*, 10, 459–465, 2020.
- Rasmussen, C. E. and Williams, C. K. I.: in: *Gaussian processes for machine learning*, The MIT Press, Cambridge, MA, 2006.
- Rasp, S., Pritchard, M. S., and Gentine, P.: Deep learning to represent subgrid processes in climate models, *Proceedings of the National Academy of Sciences*, 115, 9684–9689, 2018.
- Reichstein, M., Camps-Valls, G., Stevens, B., Jung, M., Denzler, J., Carvalhais, N., et al.: Deep learning and process under- 765 standing for data-driven Earth system science, *Nature*, 566, 195–204, 2019.
- Rong, Y., Huang, W., Xu, T., and Huang, J.: Dropedge: Towards deep graph convolutional networks on node classification, arXiv preprint arXiv:1907.10903, 2019.
- Salas, F. R., Somos-Valenzuela, M. A., Dugger, A., Maidment, D. R., Gochis, D. J., David, C. H., Yu, W., Ding, D., Clark, E. P., and Noman, N.: Towards real-time continental scale streamflow simulation in continuous and discrete space, *JAWRA* 770 *Journal of the American Water Resources Association*, 54, 7–27, 2018.
- Saunders, W.: Preparation of DEMs for use in environmental modeling analysis, *Hydrologic and Hydraulic Modeling Support*. Redlands, CA: ESRI, pp. 29–51, 2000.



- Schulthess, T. C., Bauer, P., Wedi, N., Fuhrer, O., Hoefler, T., and Schär, C.: Reflecting on the goal and baseline for exascale computing: a roadmap based on weather and climate simulations, *Computing in Science & Engineering*, 21, 30–41, 2018.
- 775 Shen, C.: A transdisciplinary review of deep learning research and its relevance for water resources scientists, *Water Resources Research*, 54, 8558–8593, 2018.
- Simley, J. D. and Carswell Jr, W. J.: The national map—hydrography, US Geological Survey Fact Sheet, 3054, 2009.
- Sun, A. Y. and Scanlon, B. R.: How can Big Data and machine learning benefit environment and water management: a survey of methods, applications, and future directions, *Environmental Research Letters*, 14, 073001, 2019.
- 780 Sun, A. Y., Scanlon, B. R., Zhang, Z., Walling, D., Bhanja, S. N., Mukherjee, A., and Zhong, Z.: Combining physically based modeling and deep learning for fusing GRACE satellite data: can we learn from mismatch?, *Water Resources Research*, 55, 1179–1195, 2019.
- Sun, A. Y., Jiang, P., Mudunuru, M. K., and Chen, X.: Explore Spatio-Temporal Learning of Large Sample Hydrology Using Graph Neural Networks, *Water Resources Research*, 57, e2021WR030394, 2021.
- 785 Tejedor, A., Longjas, A., Passalacqua, P., Moreno, Y., and Fofoula-Georgiou, E.: Multiplex networks: A framework for studying multiprocess multiscale connectivity via coupled-network theory with an application to river deltas, *Geophysical Research Letters*, 45, 9681–9689, 2018.
- Thornton, P. E., Thornton, M. M., Mayer, B. W., Wilhelmi, N., Wei, Y., Devarakonda, R., and Cook, R.: Daymet: Daily surface weather on a 1 km grid for North America, 1980–2008, Oak Ridge National Laboratory (ORNL) Distributed Active Archive Center for Biogeochemical Dynamics (DAAC, 2012).
- 790 Todini, E.: A model conditional processor to assess predictive uncertainty in flood forecasting, *International Journal of River Basin Management*, 6, 123–137, 2008.
- USGS: USGS water data retrieval library, <https://github.com/USGS-python/dataretrieval>, 2022a.
- USGS: Watershed Boundary Dataset, <https://www.usgs.gov/national-hydrography/watershed-boundary-dataset>, 2022b.
- 795 Van Beek, L., Wada, Y., and Bierkens, M. F.: Global monthly water stress: 1. Water balance and water availability, *Water Resources Research*, 47, 2011.
- Wang, X., Ji, H., Shi, C., Wang, B., Ye, Y., Cui, P., and Yu, P. S.: Heterogeneous graph attention network, in: *The world wide web conference*, pp. 2022–2032, 2019.
- Wang, Y., Jin, J., Zhang, W., Yu, Y., Zhang, Z., and Wipf, D.: Bag of tricks for node classification with graph neural networks, arXiv preprint arXiv:2103.13355, 2021.
- 800 Weerts, A., Winsemius, H., and Verkade, J.: Estimation of predictive hydrological uncertainty using quantile regression: examples from the National Flood Forecasting System (England and Wales), *Hydrology and Earth System Sciences*, 15, 255–265, 2011.
- Weiler, M., McGlynn, B. L., McGuire, K. J., and McDonnell, J. J.: How does rainfall become runoff? A combined tracer and runoff transfer function approach, *Water Resources Research*, 39, 2003.
- 805 Willard, J., Jia, X., Xu, S., Steinbach, M., and Kumar, V.: Integrating physics-based modeling with machine learning: A survey, arXiv preprint arXiv:2003.04919, 1, 1–34, 2020.
- Winnick, M. J., Carroll, R. W., Williams, K. H., Maxwell, R. M., Dong, W., and Maher, K.: Snowmelt controls on concentration-discharge relationships and the balance of oxidative and acid-base weathering fluxes in an alpine catchment, *Estuaries and Coasts*, 40, 1035–1048, 2017.
- 810



- Winsemius, H. C., Aerts, J. C., Van Beek, L. P., Bierkens, M. F., Bouwman, A., Jongman, B., Kwadijk, J. C., Ligtoet, W., Lucas, P. L., Van Vuuren, D. P., et al.: Global drivers of future river flood risk, *Nature Climate Change*, 6, 381–385, 2016.
- Wu, Z., Pan, S., Long, G., Jiang, J., and Zhang, C.: Graph wavenet for deep spatial-temporal graph modeling, arXiv preprint arXiv:1906.00121, 2019.
- 815 Xia, Y., Mitchell, K., Ek, M., Sheffield, J., Cosgrove, B., Wood, E., Luo, L., Alonge, C., Wei, H., Meng, J., et al.: Continental-scale water and energy flux analysis and validation for the North American Land Data Assimilation System project phase 2 (NLDAS-2): 1. Intercomparison and application of model products, *Journal of Geophysical Research: Atmospheres*, 117, 2012.
- Yamazaki, D., de Almeida, G. A., and Bates, P. D.: Improving computational efficiency in global river models by implementing
820 the local inertial flow equation and a vector-based river network map, *Water Resources Research*, 49, 7221–7235, 2013.
- Yang, T., Sun, F., Gentile, P., Liu, W., Wang, H., Yin, J., Du, M., and Liu, C.: Evaluation and machine learning improvement of global hydrological model-based flood simulations, *Environmental Research Letters*, 14, 114 027, 2019.
- Ye, A., Duan, Q., Yuan, X., Wood, E. F., and Schaake, J.: Hydrologic post-processing of MOPEX streamflow simulations, *Journal of hydrology*, 508, 147–156, 2014.
- 825 Yeo, I.-K. and Johnson, R. A.: A new family of power transformations to improve normality or symmetry, *Biometrika*, 87, 954–959, 2000.
- Yuval, J. and O’Gorman, P. A.: Stable machine-learning parameterization of subgrid processes for climate modeling at a range of resolutions, *Nature communications*, 11, 1–10, 2020.
- Zhang, L., Shi, Z., Han, J., Shi, A., and Ma, D.: Furcanext: End-to-end monaural speech separation with dynamic gated
830 dilated temporal convolutional networks, in: *International Conference on Multimedia Modeling*, pp. 653–665, Springer, 2020.
- Zhao, F., Veldkamp, T. I., Frieler, K., Schewe, J., Ostberg, S., Willner, S., Schauburger, B., Gosling, S. N., Schmied, H. M., Portmann, F. T., et al.: The critical role of the routing scheme in simulating peak river discharge in global hydrological models, *Environmental Research Letters*, 12, 075 003, 2017.
- 835 Zhou, J., Cui, G., Zhang, Z., Yang, C., Liu, Z., Wang, L., Li, C., and Sun, M.: Graph neural networks: A review of methods and applications, arXiv preprint arXiv:1812.08434, 2018.
- Zhu, X. and Ghahramani, Z.: Learning from labeled and unlabeled data with label propagation, 2002.